The MUSCLES Treasury Survey. IV. Scaling Relations for Ultraviolet, Ca ii K, and Energetic Particle Fluxes from M Dwarfs

The Astrophysical Journal, 843:31 (27pp), 2017 July 1 https://doi.org/10.3847/1538-4357/aa76dd

The MUSCLES Treasury Survey. IV. Scaling Relations for Ultraviolet, Ca II K, and Energetic Particle Fluxes from M Dwarfs

Allison Youngblood[1,2], Kevin France[1,2,3], R. O. Parke Loyd[1,2], Alexander Brown[3], James P. Mason[1], P. Christian Schneider[4], Matt A. Tilley[5,6,7], Zachory K. Berta-Thompson[2,3], Andrea Buccino[8,9,20], Cynthia S. Froning[10], Suzanne L. Hawley[11], Jeffrey Linsky[12], Pablo J. D. Mauas[8,9], Seth Redfield[13], Adam Kowalski[2,14], Yamila Miguel[15], Elisabeth R. Newton[16], Sarah Rugheimer[17], Antígona Segura[6,18], Aki Roberge[19], and Mariela Vieytes[8]

[1] Laboratory for Atmospheric and Space Physics, University of Colorado, 600 UCB, Boulder, CO 80309, USA; allison.youngblood@colorado.edu
[2] Department of Astrophysical and Planetary Sciences, University of Colorado, 2000 Colorado Ave., Boulder, CO 80305, USA
[3] Center for Astrophysics and Space Astronomy, University of Colorado, 389 UCB, Boulder, CO 80309, USA
[4] European Space Research and Technology Centre (ESA/ESTEC), Keplerlaan 1, 2201 AZ Noordwijk, The Netherlands
[5] Department of Earth & Space Sciences, University of Washington, Box 351310, Seattle, WA 98195, USA
[6] NASA Astrobiology Institute Virtual Planetary Laboratory, Box 351580, U.W. Seattle, WA 98195, USA
[7] Astrobiology Program, University of Washington, 3910 15th Ave. NE, Box 351580, Seattle, WA 98195, USA
[8] Dpto. de Física, Facultad de Ciencias Exactas y Naturales (FCEN), Universidad de Buenos Aires (UBA), Buenos Aires, Argentina
[9] Instituto de Astronomía y Física del Espacio (IAFE, CONICET-UBA), Casilla de Correo 67, 1428, Buenos Aires, Argentina
[10] Department of Astronomy/McDonald Observatory, C1400, University of Texas at Austin, Austin, TX 78712, USA
[11] Astronomy Department, Box 351580, University of Washington, Seattle, WA 98195, USA
[12] JILA, University of Colorado and NIST, 440 UCB, Boulder, CO 80309, USA
[13] Astronomy Department and Van Vleck Observatory, Wesleyan University, Middletown, CT 06459, USA
[14] National Solar Observatory, University of Colorado Boulder, 3665 Discovery Drive, Boulder, CO 80303, USA
[15] Observatoire de la Cote d'Azur, Boulevard de l'Observatoire, CS 34229 F-06304 NICE Cedex 4, France
[16] Massachusetts Institute of Technology, 77 Massachusetts Ave., Cambridge, MA 02138, USA
[17] School of Earth and Environmental Sciences, University of St. Andrews, Irvine Building, North Street, St. Andrews, KY16 9AL, UK
[18] Instituto de Ciencias Nucleares, Universidad Nacional Autónoma de México, México
[19] NASA Goddard Spaceflight Center, Greenbelt, MD 20771, USA

Received 2017 February 24; revised 2017 May 5; accepted 2017 May 11; published 2017 June 28

Abstract

Characterizing the UV spectral energy distribution (SED) of an exoplanet host star is critically important for assessing its planet's potential habitability, particularly for M dwarfs, as they are prime targets for current and near-term exoplanet characterization efforts and atmospheric models predict that their UV radiation can produce photochemistry on habitable zone planets different from that on Earth. To derive ground-based proxies for UV emission for use when *Hubble Space Telescope* (*HST*) observations are unavailable, we have assembled a sample of 15 early to mid-M dwarfs observed by *HST* and compared their nonsimultaneous UV and optical spectra. We find that the equivalent width of the chromospheric Ca II K line at 3933 Å, when corrected for spectral type, can be used to estimate the stellar surface flux in ultraviolet emission lines, including H I Lyα. In addition, we address another potential driver of habitability: energetic particle fluxes associated with flares. We present a new technique for estimating soft X-ray and >10 MeV proton flux during far-UV emission line flares (Si IV and He II) by assuming solar-like energy partitions. We analyze several flares from the M4 dwarf GJ 876 observed with *HST* and *Chandra* as part of the MUSCLES Treasury Survey and find that habitable zone planets orbiting GJ 876 are impacted by large Carrington-like flares with peak soft X-ray fluxes $\geqslant 10^{-3}$ W m^{-2} and possible proton fluxes $\sim 10^2$–10^3 pfu, approximately four orders of magnitude more frequently than modern-day Earth.

Key words: stars: chromospheres – stars: low-mass – Sun: flares

Supporting material: machine-readable tables

1. Introduction

1.1. UV and Ca II K Emission from M Dwarfs

Recent ultraviolet (UV) studies have shown that even optically inactive M dwarfs (i.e., those displaying Hα spectra in absorption only) display evidence of chromospheric, transition region, and coronal activity (France et al. 2013; Shkolnik et al. 2014; France et al. 2016) that may significantly affect heating and chemistry in the atmospheres of orbiting exoplanets (e.g., Segura et al. 2003, 2005; Miguel et al. 2015; Rugheimer et al. 2015; Arney et al. 2017). The Measurements of the Ultraviolet Spectral Characteristics of Low-mass Exoplanetary Systems (MUSCLES) Treasury Survey (France et al. 2016) observed seven nearby ($d < 15$ pc), optically inactive M dwarfs with known exoplanets using the *Hubble Space Telescope* (*HST*), *Chandra*, and *XMM-Newton*. All display quiescent UV emission lines and soft X-rays (SXRs) that trace hot ($T > 30{,}000$ K) plasma in the upper stellar atmosphere (Loyd et al. 2016). UV flares were observed from each M dwarf except GJ 1214, the faintest target.[21]

An M dwarf's far-UV (912–1700 Å) to near-UV (1700–3200 Å) spectrum is primarily composed of emission

[20] Visiting Astronomer, Complejo Astronómico El Leoncito, operated under agreement between the Consejo Nacional de Investigaciones Científicas y Técnicas de la República Argentina and the National Universities of La Plata, Córdoba and San Juan.

[21] The smaller flares from the MUSCLES M dwarfs show factor of <10 flux increases, which are below the signal-to-noise ratio (S/N) threshold of GJ 1214's light curves (R. O. P. Loyd et al. 2017, in preparation).

lines that form in the stellar chromosphere and transition region, with a few lines originating in the corona. There is comparatively little continuum emission due to the cool stellar photosphere ($T_{\rm eff} < 4000$ K). The H I Lyα emission line (1215.67 Å) is prominent, composing 27%–72% of the total 1150–3100 Å flux (excluding 1210–1222 Å) for the seven MUSCLES M dwarfs (France et al. 2016; Youngblood et al. 2016). The extreme-UV (EUV; 100–912 Å) stellar spectrum is currently not observable in its entirety. No current astronomical observatory exists to observe the 170–912 Å spectral range, and the ~400–912 Å range is heavily attenuated by neutral hydrogen for all stars, except the Sun. Thus, the EUV must be estimated from other proxies such as Lyα (Linsky et al. 2014) or SXRs (Sanz-Forcada et al. 2011; Chadney et al. 2015). For the M3 dwarf GJ 436, these two methods produce integrated EUV fluxes that agree within 30% (Bourrier et al. 2016; Youngblood et al. 2016).

Knowledge of an exoplanet's radiation environment is critical for modeling and interpreting its atmosphere and volatile inventory. Specifically, the spectral energy distributions (SEDs) of the host stars are essential, because molecular and atomic cross sections are strongly wavelength dependent. High-energy stellar flux heats upper planetary atmospheres and initiates photochemistry (e.g., Lammer et al. 2007; Miguel et al. 2015; Rugheimer et al. 2015; Arney et al. 2017). UV-driven photochemistry can produce and destroy potential biosignatures (O_2, O_3, and CH_4) and habitability indicators (H_2O and CO_2) in exoplanet atmospheres (Hu et al. 2012; Domagal-Goldman et al. 2014; Tian et al. 2014; Wordsworth & Pierrehumbert 2014; Gao et al. 2015; Harman et al. 2015; Luger & Barnes 2015). In particular, the ratio of far- to near-UV flux determines which photochemical reactions will dominate and thus the resultant planetary atmosphere. Compared to the Sun, M dwarfs have a far-UV/near-UV flux ratio (F(1150–1700 Å)/F(1700–3200 Å)) 100–1000 times larger, and thus most of the known O_2 false-positive mechanisms predominately impact planets orbiting M dwarfs. Accurately measuring the intrinsic Lyα flux is critical, because Lyα composes the majority of the far-UV flux. For an atmosphere with 0.02 bars of CO_2 similar to that simulated by Segura et al. (2007) with GJ 876's SED (France et al. 2012; Domagal-Goldman et al. 2014), a 20% increase (decrease) in the Lyα flux increases (decreases) the abiotic O_2 and O_3 column depths by nearly 30%.

M dwarfs are also prime targets for current and upcoming exoplanet searches and characterization efforts (see Scalo et al. 2007; Shields et al. 2016, for comprehensive overviews), due to their ubiquity in the solar neighborhood (Henry et al. 2006), high occurrence rates of small exoplanets (Dressing & Charbonneau 2015), and the larger transit and radial velocity signals their planets provide. The important UV region of an M dwarf's SED cannot yet be predicted by models, although semi-empirical modeling efforts are under way for individual stars (see Fontenla et al. 2016, and references therein). Thus, direct UV observations of individual stars are currently necessary to model and interpret planetary atmospheric observations, and the characterization of the high-energy SEDs of M dwarfs across a broad range of masses and ages is a community priority (e.g., Shkolnik & Barman 2014; France et al. 2016; Guinan et al. 2016; Bourrier et al. 2017).

Accurate UV spectral flux data are vital in understanding the salient physics and chemistry in an exoplanet atmosphere, as well as to break potential degenerate solutions in retrieval models. After *HST* and before future UV observatories begin operations, there will likely be a decade-long gap in UV observing capabilities. This gap may coincide with the majority of *TESS*'s and *CHEOPS*'s habitable zone (HZ) planet detections and subsequent study with the *James Webb Space Telescope* (*JWST*), so establishing a method of estimating UV spectral flux from ground-based proxies is imperative.

In the optical, the Ca II resonance lines at 3933 Å (Ca II K) and 3968 Å (Ca II H), the Na I D resonance lines at 5890 and 5896 Å, Hα at 6563 Å, and the Ca II infrared triplet (IRT) at 8498, 8542, and 8662 Å are known to be good indicators of stellar chromospheric activity (e.g., Walkowicz & Hawley 2009; Gomes da Silva et al. 2011; Lorenzo-Oliveira et al. 2016, and references therein). However, Hα and Na I D are only good indicators of stellar activity for very active stars (Cincunegui et al. 2007; Díaz et al. 2007; Walkowicz & Hawley 2009) and will not be considered here, because many of our target stars are optically inactive. The contrast between the Ca II H and K absorption and emission cores is larger than for the Ca II IRT, so we have limited the scope of this paper to include only one of the Ca II resonance lines. We focus on the Ca II K line at 3933 Å and ignore the Ca II H line at 3968 Å, because Hϵ is 1.6 Å redward and contaminates Ca II H at low spectral resolution.

The Ca II K line profile is a superposition of broad (>1 Å) absorption and narrow (<0.5 Å) emission. In the cooler upper photosphere, Ca^+ absorbs against the photospheric continuum, and in the hot upper chromosphere, Ca^+ emits. In the cool photospheres and lower chromospheres of M dwarfs, Ca is mostly neutral, so the Ca^+ absorption is much narrower than for solar-type stars (Fontenla et al. 2016). The Ca^+ emission traces stellar activity and has historically been measured for main-sequence stars using the Mt. Wilson S-index (Vaughan et al. 1978; Wilson 1978) and $R'_{\rm HK}$ (Noyes et al. 1984). The latter corrects the S-index for a spectral type dependence. Other methods involve isolating the emission core from the absorption by fitting and subtracting a non-LTE radiative equilibrium model to the observed spectrum (Walkowicz & Hawley 2009; Lorenzo-Oliveira et al. 2016).

For the Sun, Ca II K is known to correlate well with far-UV emission lines over the 11 yr solar cycle and to trace short-timescale variation (e.g., flares; Tlatov et al. 2015). Ca II K originates from solar features like plages and chromospheric network (Domingo et al. 2009 and references therein) and thus correlates well with the line-of-sight unsigned magnetic flux density (e.g., Schrijver et al. 1989). Ca II has also been observed to correlate with H I Lyα for M dwarfs (Linsky et al. 2013) despite significant differences between the atmospheric structures of G and M dwarfs (e.g., Mauas et al. 1997; Fontenla et al. 2016) and potentially different dynamo mechanisms (e.g., Chabrier & Küker 2006; Dobler et al. 2006; Browning 2008; Yadav et al. 2015). Other known M dwarf scaling relations include SXR–Ca II K, Hα–C IV, Hα–SXR, Hα–Mg II, Ca II K–Mg II, and correlations between Ca II K and various Balmer lines (Butler et al. 1988; Hawley & Pettersen 1991; Hawley & Johns-Krull 2003; Walkowicz & Hawley 2009). We improve on these past UV–Ca II scaling relations by increasing the size and diversity (e.g., spectral type and magnetic activity) of the M dwarf sample and expanding to more UV emission lines.

1.2. Flares and Energetic Particles

Habitability studies of M dwarf exoplanets are beginning to include estimates of stellar energetic particles (SEPs; Segura et al. 2010; Ribas et al. 2016). SEPs can be accelerated by impulsive flares where particles pass along open magnetic field lines into interplanetary space and by shock fronts associated with coronal mass ejections (CMEs; Harra et al. 2016). SEP enhancements and steady-state stellar winds can contribute significantly to planetary atmospheric loss processes by compressing an exoplanet's magnetosphere (e.g., Cohen et al. 2014; Tilley et al. 2016) and stripping atmospheric particles. SEPs, like high-energy photons, can also catalyze atmospheric chemistry. Segura et al. (2010) found that without the inclusion of particles, large UV flares do not have a long-lasting impact on an HZ planet's O_3 column density. However, including SEPs, the expected NO_x production will deplete a planet's O_3 by ~95%, requiring centuries for the O_3 column density to re-equilibrate after a flaring event ends. This can allow harmful (Voet et al. 1963; Matsunaga et al. 1991; Tevini 1993; Kerwin & Remmele 2007) or bio-catalyzing (Senanayake & Idriss 2006; Barks et al. 2010; Ritson & Sutherland 2012; Patel et al. 2015; Airapetian et al. 2016) UV radiation to penetrate to the surface.

Direct measurements of an M dwarf's energetic particle output are not currently possible, but signatures of particle acceleration in the UV and radio should be detectable in principle. Coronal dimming, when EUV emission lines dim after part of the corona has been evacuated from a CME (Mason et al. 2014), was not observed by the *Extreme UltraViolet Explorer* (*EUVE*), likely due to insufficient sensitivity. Type II radio bursts that trace shocks associated with CMEs (Winter & Ledbetter 2015) are being searched for but have not yet been detected on other stars (Crosley et al. 2016), but other possible kinematic signatures of CMEs in observed M dwarf flares have been detected (e.g., Houdebine et al. 1990; Cully et al. 1994; Fuhrmeister & Schmitt 2004). Type III radio bursts are caused by the acceleration of suprathermal electrons from solar active regions and have been detected on the M3 dwarf AD Leo (Osten & Bastian 2006). Probing the astrosphere (analogous to the heliosphere) via high-resolution Lyα measurements allows for time-averaged measurements of the stellar mass-loss rate (Wood et al. 2005a), which includes the accumulation of impulsive events (CMEs) and the quiescent stellar wind. However, it is uncertain if the kilogauss surface magnetic fields of M dwarfs would allow the acceleration of particles into the astrosphere (Osten & Wolk 2015; Drake et al. 2016). Vidotto et al. (2016) find that rapidly rotating stars may have strong toroidal magnetic fields that could prevent stellar mass loss, and Wood et al. (2014) find that the scaling relation between SXR flux and mass-loss rate breaks down for stars with SXR surface flux $>10^6$ erg cm^{-2} s^{-1}, where a fundamental change in the magnetic field topology may occur. On the Sun in 2014 October, the large active region 2192 emitted many large flares, but no CMEs. Strong overlying magnetic fields likely confined the eruption (Sun et al. 2015; Thalmann et al. 2015). As more exoplanetary atmosphere models consider the important influence of stochastic flares (Lammer et al. 2007; Segura et al. 2010; Airapetian et al. 2016; Venot et al. 2016), improving constraints on the fluxes and energies of associated particles is necessary.

To estimate SEPs for any star, we must currently rely on solar relations between SEPs and flare emission (Belov et al. 2007; Cliver et al. 2012; Osten & Wolk 2015). However, traditional flare tracers in the SXR, UV, and *U* band (3660 Å) originate from thermally heated plasma and probably do not trace particle acceleration processes; CME particles appear to be drawn nonthermally from cooler plasma in the ambient corona (Sciambi et al. 1977; Hovestadt et al. 1981). Yet, correlations between flare tracers and SEPs have been detected, likely due to Big Flare Syndrome (Kahler 1982). Big Flare Syndrome explains positive correlations between flare observables that do not share an identified physical process; for a larger total energy release from a flare, the magnitude of all flare energy manifestations will statistically be larger as well. Big Flare Syndrome occurs because a multitude of energy transport mechanisms between layers of the solar atmosphere makes energy transport efficient. These mechanisms include thermal conduction, radiation, bulk convection, and electron condensation and evaporation. For example, Belov et al. (2007) found a correlation between the Sun's 1–8 Å (1.5–12.4 keV) SXR flux and the >10 MeV proton flux, both observed simultaneously by the *Geostationary Operational Environmental Satellite* (*GOES*) system. Although likely due to Big Flare Syndrome, correlations like this are still extremely useful, because they enable an empirical means of estimating particle fluxes from observations of photons—essential for the study of distant stars.

Not all flares produce SEPs, and there may be a fundamental difference between SEP flares and non-SEP flares. Belov et al. (2005) note that an arbitrary SXR flare has a <0.4% chance of being associated with a proton enhancement, although this estimate would likely increase if it were easier to confidently identify associated flares and SEPs, but the probability increases for larger flares. The *GOES* flare classification scheme (A, B, C, M, X) is based solely on the peak 1–8 Å SXR flux as observed from Earth (1 au), and each letter represents an increased order of magnitude from 10^{-8} W m^{-2} to 10^{-3} W m^{-2} (Table 1). For example, a C3.5-class flare has a peak 3.5×10^{-6} W m^{-2} SXR flux at 1 au. Approximately 20% of C-class and ~100% of X3-class flares occur with CMEs (Yashiro et al. 2006). Thus, estimating the *GOES* flare classification of an observed stellar flare is important for estimating the probability of associated SEPs.

To estimate the SEP flux during the great AD Leo flare of 1985 (Hawley & Pettersen 1991), Segura et al. (2010) used scaling relations for active M dwarfs between broadband near-UV and 1–8 Å flare flux (Mitra-Kraev et al. 2005) and solar scaling relations between 1–8 Å flare flux and >10 MeV proton flux (Belov et al. 2005, 2007). Much of the recent UV flare data of M dwarfs have been confined to the far-UV (Loyd & France 2014; France et al. 2016), where *HST*'s COS and STIS spectrographs are most efficient, so we have developed a new method of particle flux estimation from far-UV emission line flares (Section 5).

Ideally, we would directly compare protons with a far-UV emission line directly accessible by *HST*, but high-cadence, disk-integrated, spectrally resolved far-UV observations of the Sun do not exist. To improve the method of SEP estimation from observed flares, we search for a potential correlation between energetic protons (>10 MeV) received at Earth and an EUV emission line, He II at 304 Å, which

Table 1
The *GOES* Classification Scheme of Solar Flares[a]

Class	Peak Flux at 1 au		SXR Luminosity		Solar Occurrence Rate (hr^{-1})[b]	Probability of CME[c]	Expected Peak >10 MeV Proton Flux (pfu)[d] at 1 au
	($W\ m^{-2}$)	($erg\ cm^{-2}\ s^{-1}$)	(W)	($erg\ s^{-1}$)			
X100	10^{-2}	10^{1}	2.8×10^{21}	2.8×10^{28}	$<2 \times 10^{-6}$[e]	…	…
X10	10^{-3}	10^{0}	2.8×10^{20}	2.8×10^{27}	2×10^{-5}[f]	~100%	3300
X	10^{-4}	10^{-1}	2.8×10^{19}	2.8×10^{26}	0.002	80%–100%	90
M	10^{-5}	10^{-2}	2.8×10^{18}	2.8×10^{25}	0.02	40%–80%	2
C	10^{-6}	10^{-3}	2.8×10^{17}	2.8×10^{24}	0.15	<40%	<1[f]
B	10^{-7}	10^{-4}	2.8×10^{16}	2.8×10^{23}	>0.15[g]	…	…

Notes.
[a] Classifications are based on the uncorrected *GOES* peak flare flux in the long (1–8 Å) band at 1 au. For example, a C3.5-class flare has a peak flux of 3.5×10^{-6} W m^{-2} at 1 au, and an X20-class flare has a peak flux of 2×10^{-3} W m^{-2}.
[b] Veronig et al. (2002).
[c] Yashiro et al. (2006).
[d] Cliver et al. (2012); 1 pfu = 1 proton $cm^{-2}\ s^{-1}\ sr^{-1}$.
[e] None have been observed during the *GOES* era (1976–present).
[f] Between 1991 August 25 and 2017 February 6, only five flares ⩾X10 class were observed.
[g] Below the sensitivity limits of *GOES* detectors.

Table 2
The M Dwarf Sample

No.	Star	d (pc)	R ($R_\odot$)	Spectral Type	$T_{\rm eff}$ (K)	$P_{\rm rot}$ (days)	W_λ (Ca II K) (Å)	$W_{\lambda,\rm corr}$(Ca II K) (Å)	Data Included[b]	No. of Ca II K Spectra
1	GJ 832[a]	5.0[a]	0.56[f]	M2[f]	3590[f]	45.7[q]	0.88 ± 0.09	0.73 ± 0.07	H, X, R	8
2	GJ 876[a]	4.7[a]	0.38[g]	M4[g]	3130[g]	96.7[r]	0.82 ± 0.15	0.17 ± 0.03	H, X, R, D	314
3	GJ 581[a]	6.2[a]	0.30[z,h]	M2.5[h]	3500[h]	132.5[q]	0.36 ± 0.08	0.25 ± 0.05	H	351
4	GJ 176[a]	9.3[a]	0.45[g]	M2.5[g]	3680[g]	39.5[s]	1.76 ± 0.27	1.76 ± 0.27	H, D	256
5	GJ 436[a]	10.1[a]	0.45[aa,i]	M3[i]	3420[i]	39.9[q]	0.58 ± 0.07	0.33 ± 0.04	H, D	257
6	GJ 667C[a]	6.8[a]	0.46[j]	M1.5[o]	3450[o]	103.9[q]	0.44 ± 0.11	0.27 ± 0.06	H	39
7	GJ 1214[a]	14.6[b]	0.21[k]	M4.5[o]	2820[o]	>100[t]	1.16 ± 0.2	0.040 ± 0.007	X, M	10
8	AD Leo	4.7[c]	0.44[f]	M3[f]	3410[f]	2.2[u]	11.57 ± 1.61	6.31 ± 0.88	H, R	44
9	EV Lac	5.1[a]	0.36[f]	M4[f]	3330[f]	4.38[v]	14.86 ± 2.52	6.47 ± 1.10	H	24
10	Proxima Cen[a]	1.3[d]	0.14[l]	M5.5[l]	3100[l]	83.5[w]	13.7 ± 5.93	2.50 ± 1.08	X, M, R	7
11	AU Mic	9.9[a]	0.83[m]	PMS M1[m,p]	3650[p]	4.85[x]	12.13 ± 2.17	11.44 ± 2.05	H, R	52
12	YZ CMi	6.0[a]	0.36[f]	M4[f]	3200[f]	2.78[y]	21.23 ± 4.67	5.92 ± 1.30	H, X	20
13	GJ 821	12.2[a]	0.37[f]	M2[f]	3670[f]	…	0.33 ± 0.06	0.32 ± 0.06	H	26
14	GJ 213	5.8[a]	0.25[f]	M4[f]	3250[f]	…	0.44 ± 0.12	0.15 ± 0.04	H	7
15	GJ 1132[a]	12.0[e]	0.21[n]	M4[n]	3270[n]	125[n]	1.40 ± 0.01	0.504 ± 0.005	M	1

Notes. Rotation period ($P_{\rm rot}$) uncertainties are typically ⩾10%, and effective temperature ($T_{\rm eff}$) uncertainties are typically ±100–200 K unless determined from interferometry (then ±20–100 K). We have rounded all $T_{\rm eff}$ values to the nearest 10 K.
[a] Stars with known exoplanets.
[b] (H) Keck/HIRES, (X) VLT/XSHOOTER, (R) CASLEO/REOSC, (D) APO/DIS, (M) Magellan/MIKE.
References. (a) van Leeuwen (2007), (b) Anglada-Escudé et al. (2013), (c) Jenkins (1952), (d) Lurie et al. (2014), (e) Jao et al. (2005), (f) Houdebine et al. (2016), (g) **von Braun et al. (2014), (h) **von Braun et al. (2011), (i) **von Braun et al. (2012), (j) Kraus et al. (2011), (k) Berta et al. (2011), (l) **Demory et al. (2009), (m) **White et al. (2015), (n) Berta-Thompson et al. (2015), (o) Neves et al. (2014), (p) McCarthy & White (2012), (q) Suárez Mascareño et al. (2015), (r) Rivera et al. (2005), (s) Robertson et al. (2015), (t) Newton et al. (2016), (u) Hunt-Walker et al. (2012), (v) Roizman (1984), (w) Benedict et al. (1998), (x) Vogt et al. (1983), (y) Pettersen (1980), (z) Henry et al. (1994), (aa) Hawley et al. (1996). **Interferometry measurements.
(This table is available in machine-readable form.)

has a similar formation temperature to two high-S/N lines observable in far-UV spectra (Si IV λλ1393, 1402 and He II λ1640).

This paper is organized as follows. In Section 2, we describe our sample of M dwarfs and list the sources of the observations used in this work. We also describe the reductions performed. Section 3 describes the method we used to measure the Ca II K equivalent widths of our sample of M dwarfs, and in Section 4 we present the UV–Ca II scaling relations. In Section 5 we describe the UV–proton scaling relations and their application. We present a summary of the main findings of this work in Section 6.

2. Observations and Reductions

2.1. The M Dwarf Sample

We selected stars with *HST* UV spectra and ground-based optical spectra either obtained directly by us or available in the VLT/XSHOOTER or Keck/HIRES public archives. The 15 stars that meet this criterion (listed in Table 2) are all early to

mid-M dwarfs, are nearby ($d < 15$ pc), and exhibit a broad range of rotation periods (2 to >100 days) and a broad range of ages (~10 Myr to ~10 Gyr). Nine of the 15 M dwarfs are known to host exoplanets.

Seven of the 15 stars are exoplanet host stars from the MUSCLES Treasury Survey (stars 1–7 in Table 2), and are weakly active with Hα absorption spectra and rotation periods greater than 39 days. These stars are all likely a few billion years old, and they range from M1.5 to M4.5 spectral type. We also included other weakly active M dwarfs, including MEarth planet host GJ 1132 (Berta-Thompson et al. 2015) and two stars from the "Living with a Red Dwarf" program (stars 13–15; Guinan et al. 2016). To increase the diversity in our sample, we included the well-known "flare" stars with *HST* observations (stars 8–12 in Table 2). These stars are highly active (Hα emission spectra), have short rotation periods (<7 days), and are likely young (<1 Gyr), with the exception of Proxima Centauri ($P_{\rm rot} = 83.5$ days, ~5 Gyr old; see Reiners & Basri 2008; Davenport et al. 2016).

2.2. M Dwarf UV and Optical Data

A goal of the MUSCLES Treasury Survey was to obtain ground-based optical spectra contemporaneous with the *HST* UV observations. Scheduling changes and weather did not allow for any truly simultaneous UV–optical observations, but several targets have spectroscopic data obtained with the Dual Imaging Spectrograph (DIS) on the ARC 3.5 m telescope at Apache Point Observatory (APO) or the REOSC echelle spectrograph on the 2.15 m telescope at Complejo Astronómico El Leoncito (CASLEO) within a day or two of the *HST* observations. We also gathered spectra of GJ 1132, GJ 1214, and Proxima Cen on the nights of 2016 March 7–9 using the MIKE echelle spectrograph on the Magellan Clay telescope. Because M dwarfs are prime targets of radial velocity exoplanet searches, there is a wealth of high-resolution Ca II spectra in the public archives of major observatories, including VLT and Keck. The archival spectra compose the bulk of our Ca II measurements.

APO/DIS ($R \sim 2500$) and CASLEO/REOSC ($R \sim 12{,}000$) spectra were reduced using standard IRAF[22] routines. See details in Cincunegui & Mauas (2004) for CASLEO reductions and Cincunegui et al. (2007) and Buccino et al. (2014) for presentation of some of the Proxima Cen and AD Leo observations. Magellan/MIKE spectra ($R \sim 25{,}000$) were reduced using the standard MIKE pipeline included in the Carnegie Python Distribution (CarPy). Science-level VLT/XSHOOTER ($R \sim 6000$) data products were obtained from the ESO Science Archive Facility, and Keck/HIRES ($R \sim 60{,}000$) pipeline-reduced spectra were obtained from the KOA archive. As we are interested in looking at as many spectra as possible and measuring only equivalent widths of the Ca II K line, the pipeline-extracted spectra using `MAKEE`[23] suit our purposes well. We did not use spectra where the automatic extraction failed or the wavelength calibration was incorrect. We also did not co-add the adjacent orders on which Ca II K appears, but instead averaged the equivalent width measurements (Section 3) from each order to create one equivalent width measurement per echellogram.

The *HST* UV spectra were obtained either from the MAST online archive, including the MUSCLES High-Level Science Products[24] (HLSPs; Loyd et al. 2016), or the StarCAT portal.[25] GJ 1132's (star 15) STIS G140M spectrum was obtained on 2016 February 13. For the seven MUSCLES M dwarfs (stars 1–7), the UV line fluxes come from Youngblood et al. (2016) and France et al. (2016). The UV emission lines of stars 8–14 were directly measured from archival *HST* spectra or obtained from Wood et al. (2005b).

For AD Leo (star 8) and Proxima Centauri (star 10), we reconstructed the Lyα profiles using the methods described in Youngblood et al. (2016). Proxima Cen's reconstruction is included as part of a 5 Å–5.5 μm SED on the MUSCLES HLSP website.[26] The differences between our Lyα reconstructions and those presented in Wood et al. (2005b) are small, ~20% in integrated Lyα flux for AD Leo and ~4% in integrated Lyα flux for Proxima Cen. We also reconstructed the Lyα profile of GJ 1132 (star 15; $F(\mathrm{Ly}\alpha) = (2.64^{+2.58}_{-0.65}) \times 10^{-14}$ erg cm^{-2} s^{-1}) for the first time using the methods from Youngblood et al. (2016). Note that the Lyα error bars have been averaged for symmetry in Table 3. All UV fluxes used in this work are shown in Table 3.

2.2.1. Interstellar Medium Corrections

Five out of nine of our UV emission lines (Lyα, Mg II, C II, Si II, and Si III) are affected by absorption from the interstellar medium (ISM), and here we describe our attempts to mitigate the effect of ISM absorption on our measurements. All the reported Lyα fluxes have been reconstructed from the wings of the observed line profile using the technique described in Youngblood et al. (2016) or Wood et al. (2005b) for EV Lac. The Mg II fluxes were corrected uniformly for a 30% ISM absorption, assuming a typical $\log_{10} N(\mathrm{Mg\ II}) \sim 13$ for stars within 20 pc (Redfield & Linsky 2002). Many of the Mg II observations are not sufficiently resolved to allow for a profile reconstruction, and we do not apply a correction factor scaling either with distance or H I column densities measured along the line of sight, because the Mg^+ abundance varies in the local ISM. C II λ1334 is the most significantly impacted of the C II $\lambda\lambda$1334, 1335 doublet, and so we excluded its contribution from the reported C II fluxes.

We do not apply ISM corrections to the Si II (see Redfield & Linsky 2004, for a discussion of Si II absorption in the local ISM) or Si III fluxes, noting that the ISM's effect on Si III is likely small. The intrinsic narrowness of the M dwarf emission lines may mean that for some sightlines, the ISM absorption coincides with the stellar emission line, but for others the ISM absorption is shifted away from the emission, and the line's flux is not attenuated. Ca^+ from the ISM can significantly attenuate Ca II H and K, but only for distant stars ($d > 100$ pc; Fossati et al. 2017). Because all of our targets are within 15 pc, Ca II ISM absorption is likely negligible, and we do not apply a correction.

[22] IRAF is distributed by the National Optical Astronomy Observatory, which is operated by the Association of Universities for Research in Astronomy, Inc., under cooperative agreement with the National Science Foundation.
[23] http://www.astro.caltech.edu/~tb/makee/
[24] https://archive.stsci.edu/prepds/muscles/
[25] http://casa.colorado.edu/~ayres/StarCAT/
[26] https://archive.stsci.edu/prepds/muscles/

Table 3
UV Emission Line Fluxes of the M Dwarf Sample

No.	Star	Si III	$\sigma_{\text{Si III}}$	Lyα[b]	$\sigma_{\text{Ly}\alpha}$[b]	Si II	$\sigma_{\text{Si II}}$	C II	$\sigma_{\text{C II}}$	Mg II	$\sigma_{\text{Mg II}}$
1	GJ 832[a]	2.55E–15	6.33E–17	9.50E–13	6.00E–14	7.65E–16	6.33E–17	3.78E–15	8.18E–17	1.84E–13	2.02E–15
2	GJ 876[a]	8.11E–15	1.01E–16	3.90E–13	4.00E–14	1.19E–15	7.06E–17	1.06E–14	1.26E–16	3.11E–14	9.31E–16
3	GJ 581[a]	2.94E–16	3.54E–17	1.10E–13	3.00E–14	7.93E–17	4.41E–17	4.81E–16	4.26E–17	1.88E–14	7.54E–16
4	GJ 176[a]	2.15E–15	5.84E–17	3.90E–13	2.00E–14	7.34E–16	6.49E–17	5.43E–15	9.66E–17	1.56E–13	1.53E–15
5	GJ 436[a]	5.15E–16	4.00E–17	2.10E–13	3.00E–14	1.87E–16	4.47E–17	1.09E–15	5.85E–17	3.84E–14	1.01E–15
6	GJ 667C[a]	5.07E–16	3.91E–17	5.20E–13	9.00E–14	1.29E–16	6.13E–17	6.50E–16	4.63E–17	4.12E–14	1.10E–15
7	GJ 1214[a]	8.05E–17	2.77E–17	1.30E–14	1.00E–14	1.36E–17	2.09E–17	9.83E–17	3.00E–17	1.66E–15	2.70E–16
8	AD Leo	1.41E–13	8.88E–16	8.07E–12	2.00E–13	1.64E–14	2.58E–16	1.66E–13	4.83E–16	2.79E–12[c]	2.79E–13[c]
9	EV Lac	3.86E–14	1.46E–15	2.75E–12[c]	5.50E–13[c]	2.49E–15	4.95E–16	3.76E–14	6.42E–16	…	…
10	Proxima Cen[a]	2.03E–14	7.57E–16	4.37E–12	7.00E–14	2.14E–15	2.08E–16	2.61E–14	2.79E–16	…	…
11	AU Mic	8.78E–14	3.45E–16	1.07E–11	4.00E–13	1.09E–14	8.97E–17	1.44E–13	1.81E–16	4.20E–12[c]	4.20E–13[c]
12	YZ CMi	…	…	…	…	…	…	…	…	1.10E–12	1.42E–15
13	GJ 821	5.58E–16	6.56E–16	…	…	9.52E–17	9.52E–18	1.05E–16	2.89E–17	2.62E–14	2.69E–15
14	GJ 213	…	…	…	…	1.62E–16	1.62E–17	2.32E–16	2.32E–17	7.13E–15	2.30E–15
15	GJ 1132[a]	…	…	2.64E–14	1.62E–14	…	…	…	…	…	…

No.	Star	Si IV	$\sigma_{\text{Si IV}}$	He II	$\sigma_{\text{He II}}$	C IV	$\sigma_{\text{C IV}}$	N V	$\sigma_{\text{N V}}$	EUV[e]
1	GJ 832[a]	3.33E–15	9.19E–17	6.81E–15	2.93E–16	7.64E–15	2.88E–16	3.51E–15	7.54E–17	8.65E–13
2	GJ 876[a]	8.44E–15	1.36E–16	5.51E–15	2.92E–16	2.29E–14	4.34E–16	1.07E–14	1.26E–16	3.43E–13
3	GJ 581[a]	4.44E–16	6.71E–17	7.22E–16	1.90E–16	1.84E–15	1.84E–16	5.34E–16	4.48E–17	1.01E–13
4	GJ 176[a]	2.30E–15	8.64E–17	6.73E–15	3.03E–16	1.23E–14	2.83E–16	3.10E–15	7.56E–17	3.57E–13
5	GJ 436[a]	6.81E–16	6.92E–17	1.50E–15	2.13E–16	2.39E–15	1.76E–16	9.56E–16	5.04E–17	1.90E–13
6	GJ 667C[a]	8.25E–16	7.17E–17	1.94E–15	2.25E–16	2.97E–15	2.05E–16	7.16E–16	5.31E–17	4.73E–13
7	GJ 1214[a]	4.79E–17	3.74E–17	7.43E–17	1.44E–16	5.23E–16	1.21E–16	1.84E–16	3.58E–17	1.29E–14
8	AD Leo	1.74E–13	5.39E–16	3.02E–13	9.45E–16	5.66E–13	1.21E–15	1.41E–13	5.89E–16	8.16E–12
9	EV Lac	1.82E–14	9.76E–16	7.41E–14	1.58E–15	1.41E–13	1.96E–15	3.91E–14	9.03E–16	2.60E–12
10	Proxima Cen[a]	2.72E–14	3.83E–16	3.08E–14	5.87E–16	1.38E–13	9.13E–16	4.00E–14	4.56E–16	3.86E–12
11	AU Mic	9.53E–14	1.63E–16	2.75E–13	3.50E–16	3.55E–13	3.85E–16	7.42E–14	1.82E–16	1.42E–11
12	YZ CMi	…	…	…	…	…	…	…	…	…
13	GJ 821	8.16E–17	4.29E–17	6.84E–16	2.53E–16	6.69E–16	1.90E–16	1.95E–16	1.95E–17	…
14	GJ 213	2.13E–16	2.13E–17	2.57E–16	2.57E–17	5.22E–16	1.55E–16	3.58E–16	3.58E–17	…
15	GJ 1132[a]	…	…	…	…	…	…	…	…	2.31E–14

Notes. All emission-line fluxes are as observed from Earth (erg cm^{-2} s^{-1}). All flux measurements for stars 1–7 come from Youngblood et al. (2016) and France et al. (2016). The Lyα reconstructed flux for AU Mic also comes from Youngblood et al. (2016). All other measurements are from this work, except where noted.
[a] Stars with known exoplanets.
[b] Reconstructed Lyα fluxes. Asymmetric error bars from Youngblood et al. (2016) have been averaged.
[c] Wood et al. (2005b).
[e] Calculated using the reconstructed Lyα fluxes (Table 3) and scaling relations from Linsky et al. (2014), which have been re-shown in Table 6.

(This table is available in machine-readable form.)

2.3. Solar X-Ray, UV, and Proton Data

We utilize time-series solar irradiance (disk-integrated) measurements from the Extreme ultraviolet Variability Experiment (EVE) suite of instruments on board the *Solar Dynamics Observatory* (*SDO*; Woods et al. 2012). We use the He II (304 Å) irradiance from the 2010–2014 era from the MEGS-A channel (50–370 Å with 1 Å spectral resolution). MEGS-A operates at a 10 s cadence, but we use 1-minute averages in this work to reduce noise.

Time-series solar SXR irradiance measurements and in situ proton measurements come from the *Geostationary Operational Environmental Satellite* (*GOES*) system.[27] SXRs are measured in a 1–8 Å (1.5–12.4 keV) band. Note that we do not divide the *GOES* 1–8 Å flux by 0.7, the recommended correction factor, to obtain absolute flux units. This is because we utilize the *GOES* SXR flare classification scheme below, which operates on data that have not been corrected, and recent SXR observations with the MinXSS cubesat suggest that this correction factor is incorrect (Woods et al. 2017). We utilize the proton measurements from the >10 MeV and >30 MeV channels.

[27] https://www.ngdc.noaa.gov/stp/satellite/goes/index.html

3. Ca II K Equivalent Widths

To isolate the chromospheric Ca II K emission line so we can compare it to the UV emission line fluxes, we must correct for the absorption by subtracting a radiative equilibrium model. This is particularly important for the low-resolution spectra, which typically cannot resolve the emission cores. Only the CASLEO/REOSC spectra are flux calibrated, so to be consistent with the rest of the spectra, we normalized the flux in the isolated Ca II K emission core to nearby continuum, making this measurement akin to an equivalent width. Busà et al. (2007), Marsden et al. (2009), and Walkowicz & Hawley (2009) used this "residual" equivalent width technique in their analyses of Ca II lines. Note that we do not use the widely used S-index (Vaughan et al. 1978; Wilson 1978) or R'_{HK} index

(e.g., Noyes et al. 1984), because for our medium-resolution spectra the Hϵ emission line is blended with the Ca II H emission core line.

The residual equivalent width W_λ is given by

$$W_\lambda = \frac{\int_{\lambda_1}^{\lambda_2} F_{\rm observed}\, d\lambda - \int_{\lambda_1}^{\lambda_2} F_{\rm PHOENIX}\, d\lambda}{\overline{F}_{\rm continuum}}. \quad (1)$$

$F_{\rm observed}$ is the observed Ca II K profile, $F_{\rm PHOENIX}$ is the radiative equilibrium PHOENIX model (Husser et al. 2013) scaled to $F_{\rm observed}$ in the Ca II K absorption wings, λ_1 and λ_2 are the interactively chosen bounds of integration around the narrow chromospheric Ca II K emission, and $\overline{F}_{\rm continuum}$ is the average observed flux in the continuum region (before subtraction of the PHOENIX model) from 3937 to 3940 Å. We selected the 3937–3940 Å region for continuum normalization because it is close to the Ca II K line (3933 Å), and the spectral response curves of the various CCDs we are using are unlikely to vary significantly over ~7 Å. Walkowicz & Hawley (2009) and Rauscher & Marcy (2006) normalize their effective equivalent widths using continuum regions 3952.8–3956.0 Å and 3974.8–3976.0 Å. We do not believe that there is a significant difference between these continuum choices, because neither are truly continuum, due to the high density of absorption lines in this spectral region.

The PHOENIX models were retrieved from the Husser et al. (2013) grid using literature values for $T_{\rm eff}$ (Table 2) and assuming $\log_{10} g = 5$ and [Fe/H] = 0 (solar). However, for the seven MUSCLES targets, we use the PHOENIX models incorporated into the high-level science products available on MAST. See Loyd et al. (2016) for details about the parameters used to retrieve these models. The PHOENIX models have resolution $R = 500{,}000$ around Ca II K (Husser et al. 2013) and were convolved with a Gaussian kernel to match the resolution of the spectra from the various instruments used (Section 2). The PHOENIX models were also shifted in velocity space to the rest frame of each target before fitting. We scaled the PHOENIX spectra to match three points in the broad Ca II K absorption wings.

The M dwarfs in our sample have a broad range of effective temperatures, so we must account for a dependence on spectral type in this residual equivalent width measurement (see Appendix A for more details on the following description). Stars of earlier spectral type have brighter continuum fluxes than later-type stars, affecting the normalization of the emission core's flux. Walkowicz & Hawley (2009) restricted their Ca II analysis to a single spectral subtype (M3 V) to avoid the issue of a spectral type dependence. To correct the residual equivalent widths (W_λ from Equation (1)) for spectral type dependence, we normalized to the W_λ value for a reference star parameterized by $T_{\rm eff} = 3680$ K, log $g = 5$, and [Fe/H] = 0. The normalization or "correction" factor is the ratio of the star's average continuum flux and the reference star's average continuum flux. Both continuum averages come from the PHOENIX models. The corrected residual equivalent width is given by

$$W_{\lambda,\rm corr} = W_\lambda \times \frac{x(T)}{x(3680\ {\rm K})}. \quad (2)$$

Here $x(T)$ is the average continuum flux value from 3936.9 to 3939.9 Å from a PHOENIX model for a star with temperature T, and $x(3680\ {\rm K})$ is the PHOENIX model's average continuum flux value for the reference star. The reference star's effective temperature corresponds to GJ 176 and was chosen arbitrarily. To find the continuum values, $x(T)$, we used a grid of PHOENIX models from $T_{\rm eff} = 2400$ K to $T_{\rm eff} = 4000$ K, all with $\log_{10} g = 5$ and [Fe/H] = 0 (solar). We fit a cubic spline function to the average flux values in the 3936.9–3939.9 Å region to determine the correction factor $x(T)/x(3680\ {\rm K})$ (Table 4, Figure 1). The uncertainty in $W_{\lambda,\rm corr}$ introduced by the correction factor has two roughly equivalent sources: the uncertainty in $T_{\rm eff}$ and the assumption of $\log_{10} g = 5$ and [Fe/H] = 0 for all our stars. Uncertainties in $T_{\rm eff}$ are likely 100–200 K, and this translates to a ~20% uncertainty in the correction factor at the high-temperature end ($T_{\rm eff} = 3700$ K), to ~70% uncertainty around $T_{\rm eff} = 3000$ K, and to ~100% uncertainty at the low-temperature end

Table 4
Correction Factors for Calculating $W_{\lambda,\rm corr}$ (Equation (2))

T	$x(T)/x(3680\ {\rm K})$	T	$x(T)/x(3680\ {\rm K})$
2400	1.1613×10^{-3}	3300	0.39680
2500	2.5175×10^{-3}	3400	0.53075
2600	5.6663×10^{-3}	3500	0.68191
2700	1.2907×10^{-2}	3600	0.85061
2800	2.9381×10^{-2}	3700	1.0425
2900	5.9956×10^{-2}	3800	1.2642
3000	0.11061	3900	1.5233
3100	0.18269	4000	1.8277
3200	0.27899		

Note. To calculate the correction factors $x(T)/x(3680\ {\rm K})$, we computed $x(T)$, the average stellar surface flux values from 3936.9 to 3939.9 Å for PHOENIX models from the Husser et al. (2013) grid for a range of temperatures T (K), all with $\log_{10} g = 5$ and [Fe/H] = 0 (solar). From a cubic spline fit to the $x(T)$ values, we find $x(3680\ {\rm K}) = 7.7453 \times 10^{12}$ erg cm^{-2} s^{-1} cm^{-1}.

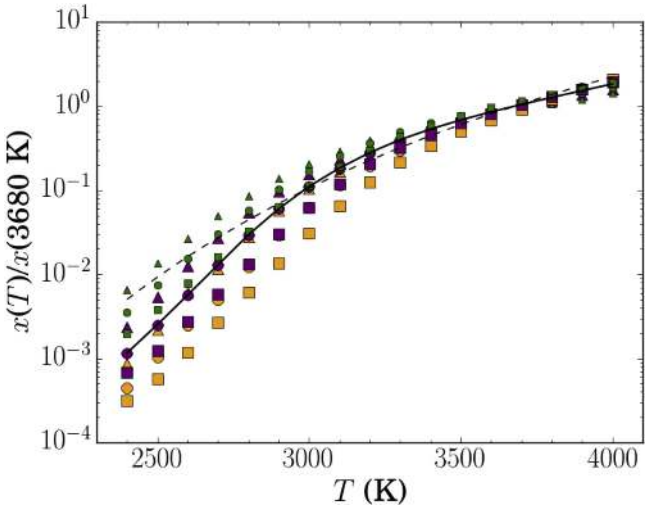

Figure 1. Correction factor $x(T)/x(3680\ {\rm K})$ used for calculating $W_{\lambda,\rm corr}$ from W_λ as a function of stellar effective temperature T (Equation (2)). The solid black curve shows the cubic spline fit to the purple circles, which correspond to the data in Table 4. This figure shows the spread in correction factor values when varying metallicity and surface gravity. Purple represents [Fe/H] = 0, orange [Fe/H] = −0.5, and green [Fe/H] = +0.5. The circles represent $\log_{10} g = 5.0$, triangles $\log_{10} g = 4.5$, and squares $\log_{10} g = 5.5$. The dashed black curve shows a correction factor based on a blackbody curve.

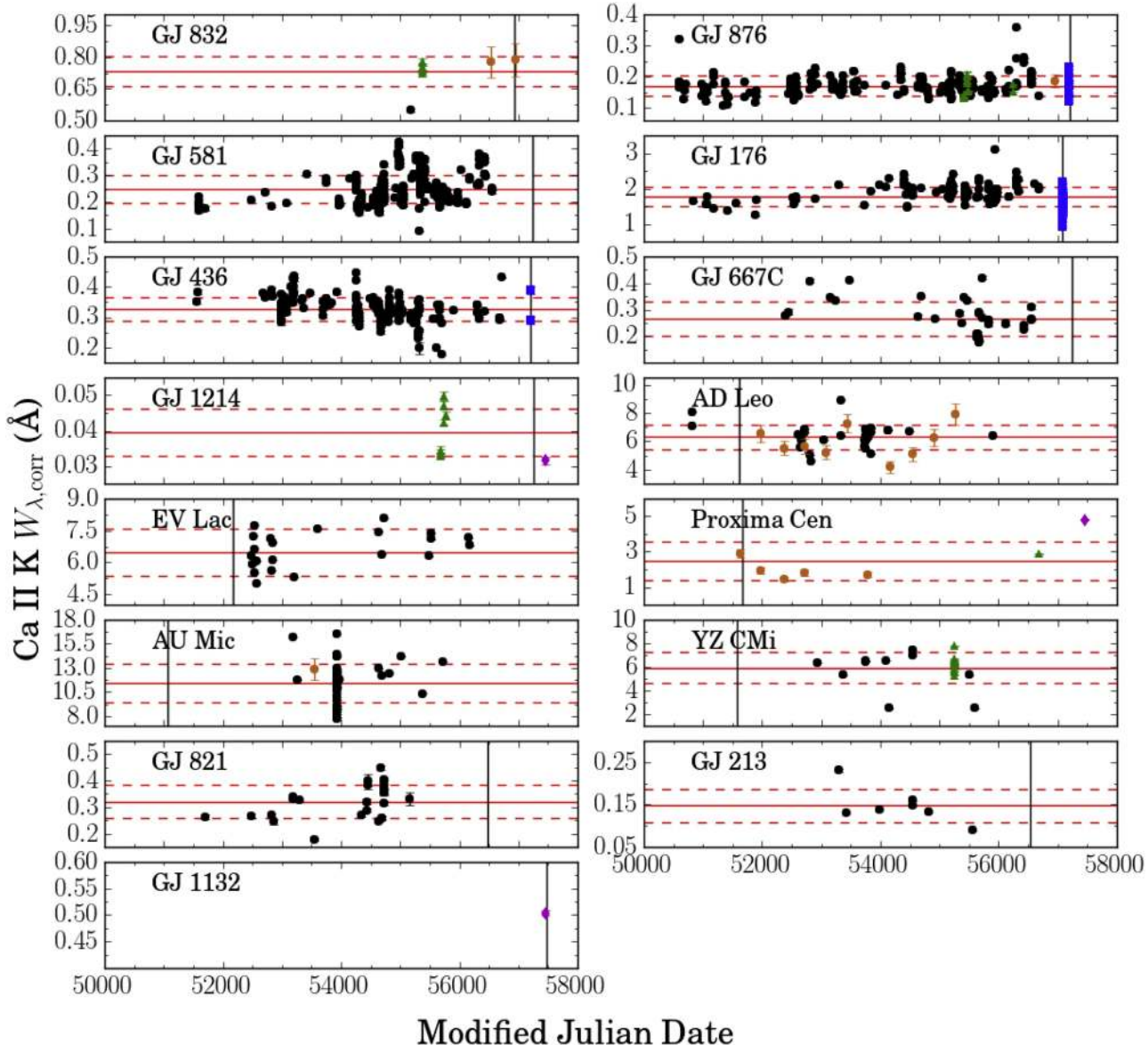

Figure 2. Ca II K equivalent width ($W_{\lambda,\mathrm{corr}}$) light curves for our M dwarf sample displayed over the time period 1995 October 10–2017 September 4 (Modified Julian Date = 50,000–58,000). The solid horizontal red line shows the mean equivalent width, and the two dashed red lines show the standard deviation of the data. The vertical solid black lines show the dates of the UV observations used in this work (see Section 4.2 and Table 3). The black circles represent data from Keck/HIRES, green triangles are VLT/XSHOOTER, orange circles are CASLEO/REOSC, magenta diamonds are Magellan/MIKE, and blue squares are APO/DIS. 1σ photometric error bars are shown, but they are typically smaller than the data points.

($T_{\mathrm{eff}} = 2400$ K). The surface gravity of our M dwarf sample ranges from ~4.75 to 5.0, and given the coarseness of the PHOENIX grids, $\log_{10} g = 5$ is a good assumption. The metallicity ranges from −0.5 to 0.5, but [Fe/H] = 0 is valid for most of the M dwarfs in our sample. Examining the average flux values in the 3936.9–3939.9 Å region for PHOENIX models sampling a range of surface gravity and metallicity values, we find that the dispersion in $x(T)/x(3680\ \mathrm{K})$ values for a given temperature is of similar magnitude to the dispersion in $x(T)/x(3680\ \mathrm{K})$ values (assuming $\log_{10} \mathrm{g} = 5$ and [Fe/H] = 0) between $\Delta T_{\mathrm{eff}} = 200$ K bins (Figure 1).

We also examined the effect of PHOENIX model parameters on $W_{\lambda,\mathrm{corr}}$ during the model subtraction and the effect of interactively choosing the integration limits. Using a single Keck/HIRES spectrum and three PHOENIX model spectra, we measured $W_{\lambda,\mathrm{corr}}$ 30 times and compared to the "true" measurement for that spectrum and its photometric error bar (the true measurements are shown in Figure 2 and used to calculate the equivalent width values reported in Table 2). We find that the PHOENIX model chosen for subtraction has a negligible effect on the equivalent width measurements, but that the uncertainty introduced from differences in the interactively chosen integration bounds is slightly larger than the photometric uncertainty. We do not correct the photometric error bars on the individual equivalent width measurements, and the error bars reported in Table 2 come from the dispersion in the many equivalent width measurements made for each target (described fully in Section 4.1).

4. UV–Ca II Relation

In this section we present scaling relations between Ca II K and far- and near-UV emission lines, as well as the

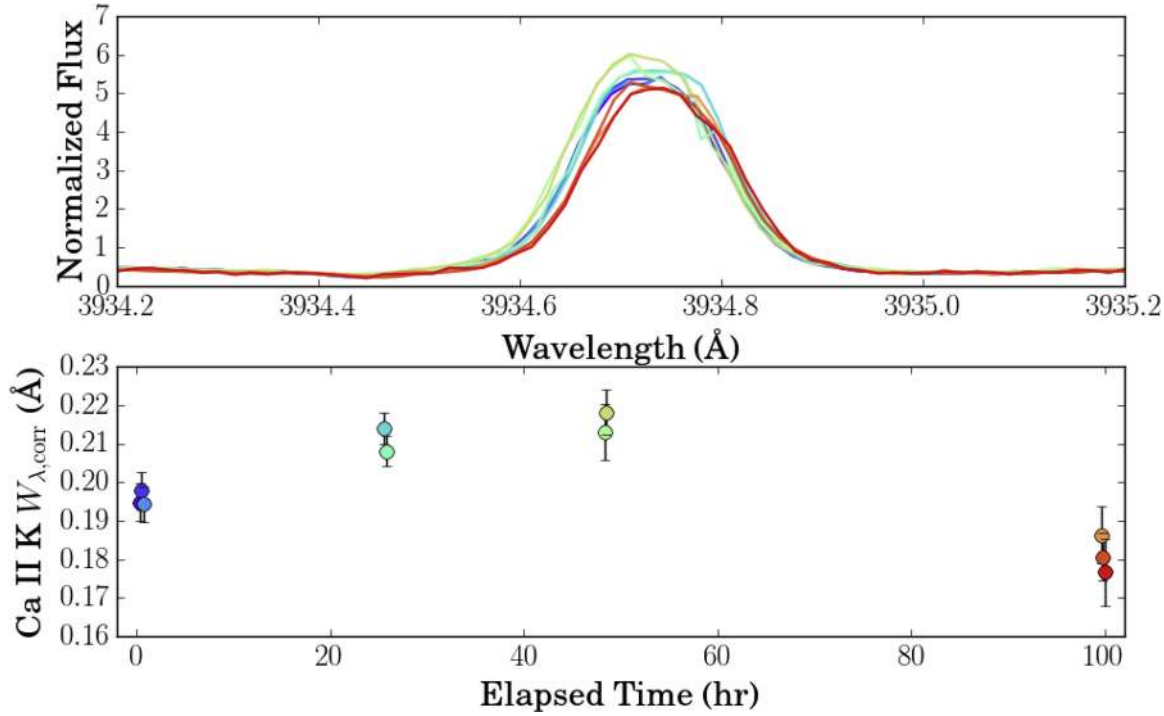

Figure 3. Top panel: normalized line profiles of the Ca II K line for GJ 876 over the course of 4 days as observed by Keck/HIRES 2013 September 13–17. The apparent redshift in the line centroid is likely an artifact from the MAKEE automated wavelength calibration. Bottom panel: Ca II K corrected equivalent widths over the course of the 4 days. The colors correspond to the line colors in the top panel.

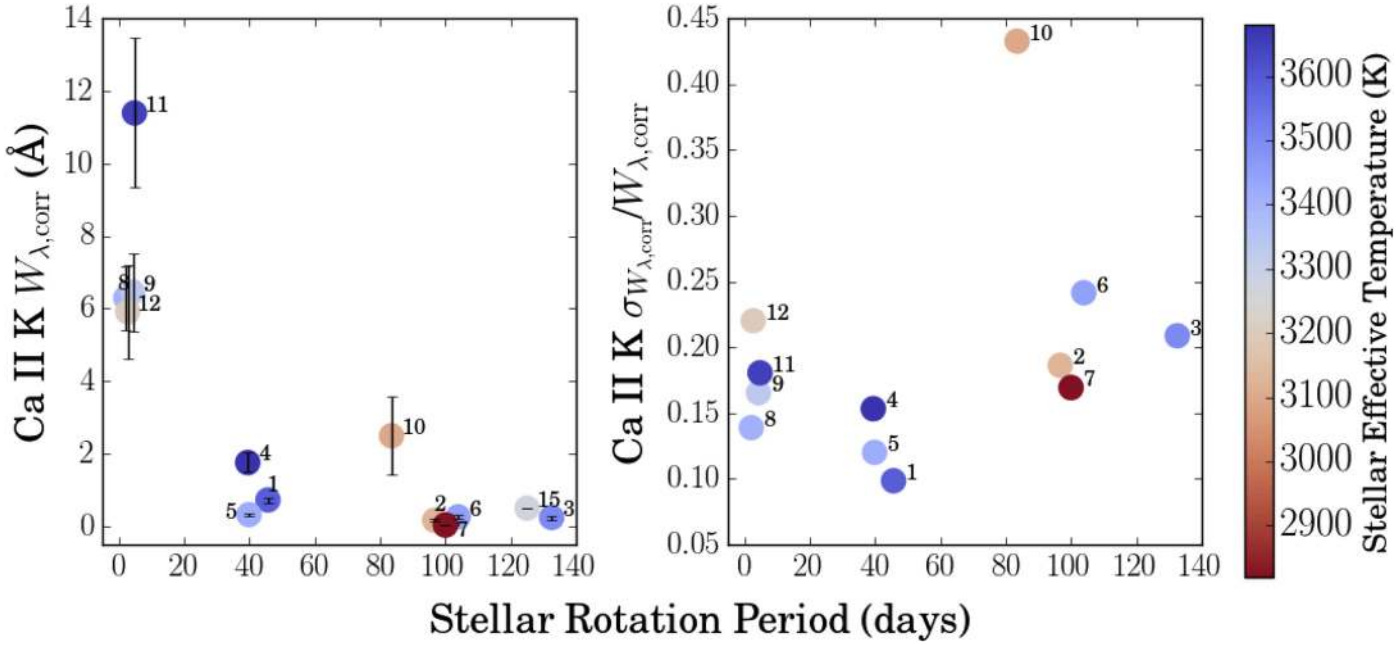

Figure 4. Stellar rotation period in days compared to the corrected Ca II K equivalent widths (left panel) and the normalized scatter in the equivalent widths (right panel). Note that GJ 1132 (star 15) is not included in the right panel, because it only has one Ca II K measurement, and GJ 821 (star 13) and GJ 213 (star 14) are not included in either panel, because they do not have P_{rot} measurements.

total EUV flux (100–912 Å). See Appendix B for a presentation of scaling relations between the far- and near-UV emission lines themselves.

4.1. Ca II K Variability

A total of 10 out of 15 members of our M dwarf sample have tens to hundreds of archival Ca II K observations, and we derived our equivalent width measurements from all the spectra to avoid biases from stellar activity on all timescales (i.e., flares, rotation, stellar magnetic activity cycle). Equivalent width light curves are shown in Figure 2 for the 15 stars. Variability is observed, especially over the course of a few days, but no definitive signs of cyclic activity due to stellar rotation or the stellar dynamo are observed, nor are they ruled out. Approximately 20% spreads in the Ca II K equivalent

widths are typically observed over the course of a few days (see Figures 3 and 4) and are likely due to flares and rotation of starspots into and out of view. Figure 3 shows the evolution of the Ca II K emission profile for GJ 876 over the course of 4 days and the corresponding change in the corrected Ca II K equivalent widths.

For each target, we computed a mean Ca II K equivalent width with an uncertainty equal to the standard deviation of the measurements (Table 2). GJ 1132 has only one equivalent width measurement, so the photometric error bar was reported for that measurement. The averages from stars with few observations could be strongly skewed if they coincide with an unresolved episode of high activity. The targets with the fewest observations are GJ 832, GJ 1214, GJ 1132, Proxima Cen, and GJ 213 (see Section 2 and Table 2 for the list of sources for our optical spectra).

Figure 4 shows the demographics of our sample (stellar rotation period $P_{\rm rot}$ and effective temperature $T_{\rm eff}$) compared to the corrected Ca II K equivalent widths and the observed scatter in those values. In general, the fast rotators ($P_{\rm rot} < 7$ days) have the largest equivalent widths. Unsurprisingly, these stars are the well-known flare stars AD Leo, EV Lac, AU Mic, and YZ CMi, and they are also the youngest stars (<1 Gyr) in the sample. Between $P_{\rm rot} \sim 40$ and 85 days, most stars exhibit small equivalent widths, but Proxima Cen (star 10) and GJ 176 (star 4) are outliers. West et al. (2015) find that late M dwarfs (M5–M8) rotating faster than 86 days and early M dwarfs (M0–M4) rotating faster than 26 days exhibit greater optical activity (i.e., an Hα emission spectrum and greater Ca II equivalent width; Walkowicz & Hawley 2009). Proxima Cen meets this optical activity criterion, but GJ 176 does not. However, even the "optically inactive" stars (Hα absorption spectrum) in our sample exhibit UV activity.

The right panel of Figure 4 shows the scatter observed in the Ca II K $W_{\lambda,\rm corr}$ light curves normalized to $W_{\lambda,\rm corr}$. The scatter ranges from ~10% to 25% (although Proxima Cen's scatter is 43%), with no clear dependence on $T_{\rm eff}$ and a possible positive correlation with $P_{\rm rot}$, although our sample is sparse for $T_{\rm eff} < 3200$ K and $P_{\rm rot} > 60$ days.

4.2. UV–Optical Correlations

For our 15 M dwarf sample, we compare the average Ca II K corrected equivalent widths ($W_{\lambda,\rm corr}$) reported in Table 2 with UV emission line surface fluxes. By using the corrected Ca II K equivalent width (Section 3) and UV surface fluxes, we attempt to minimize spectral type dependences in our results. We note, however, that the uncertainties in the stellar radii (used to compute the stellar surface flux) are large, and there may be a systematic bias for the lowest-mass stars. Direct interferometric measurements yield vastly different radii for mid-M dwarfs of similar effective temperatures; in particular, directly measured radii are tens of percent larger than radii determined by indirect means (von Braun et al. 2014). The nine UV lines we used for comparison are listed with their formation temperatures in Table 5.

Figure 5 shows the correlations between $W_{\lambda,\rm corr}$ and surface flux ($F_{\rm S,UV}$) for nine UV emission lines and the EUV flux, which is derived from Lyα (see Section 4.2.1), with their power-law fits of the form $\log_{10} F_{\rm S,UV} = (\alpha \times \log_{10} W_{\lambda,\rm corr}) + \beta$ (Table 5). We find statistically significant correlations between Ca II K and all nine UV emission lines, which have formation temperatures ranging from 30,000 to 160,000 K. As expected, the correlations with the least scatter are for Mg II and Lyα (0.27 and 0.18 dex, respectively), both optically thick lines with formation temperatures similar to Ca II K. Ca II has been previously found to correlate positively with Lyα (Linsky et al. 2013) and Mg II (Walkowicz & Hawley 2009). Note that due to the large uncertainty in GJ 1214's Lyα flux (Youngblood et al. 2016), we do not include it in the fit, although its effect on the fit is small. GJ 1214 is an outlier from the fits for all nine UV lines, and GJ 876 is a significant outlier for all but Mg II and Lyα. Of the seven MUSCLES M dwarfs, GJ 876 exhibited the most frequent and largest flares. These flares were observed in all lines except Mg II and Lyα, which were observed on different *HST* visits from the other far-UV emission lines, so GJ 876's apparently elevated UV surface fluxes in Figure 5 may be due to these flares. There is no clear dependence on fit quality (as measured by the Pearson correlation coefficients or the standard deviation of the fit) with the formation temperature of the UV line.

By eye, it appears that some of the Ca II–UV correlations in Figure 5 may be better fit by two power laws with a break around $W_{\lambda,\rm corr} \approx 1$, the transition in this data set between the "inactive" ($W_{\lambda,\rm corr} \lesssim 1$) and "active" ($W_{\lambda,\rm corr} \gtrsim 1$) M dwarfs. In the Ly$\alpha$ and EUV panels in Figure 5, we show two power-law fits in addition to the single power-law fit. As with the single power-law fits, GJ 1214 is excluded. The broken power-law fits indicate that for these two UV surface fluxes, the Ca II–UV correlations become approximately constant at low stellar activity (Table 5). Greater study of the low-activity M dwarfs is necessary to determine whether the UV fluxes become approximately constant in that regime, as the apparent flattening of many of the correlations is largely due to a single star: GJ 1214.

4.2.1. Estimating the EUV Spectrum from Ca II K

Predicting an M dwarf's Lyα flux is important not only because Lyα constitutes a major fraction of the far-UV flux, but also because it is a means for estimating the EUV spectrum, which currently cannot be observed for any star except the Sun. In Figure 5 and Table 5, we have determined the scaling relation between the total EUV flux (100–912 Å) and $W_{\lambda,\rm corr}$ for our stars. The fit is very similar to the Lyα–Ca II K best-fit line, because the EUV fluxes were derived from scaling relations with Lyα from Linsky et al. (2014).

In Table 6, we substitute our Ca II–Lyα scaling relation into the Lyα–EUV scaling relations in Table 5 of Linsky et al. (2014) to allow the reader to directly reconstruct the EUV spectrum from a Ca II K $W_{\lambda,\rm corr}$ measurement. We have also re-shown the scaling relations from Linsky et al. (2014) in Table 6, although they have been simplified for brevity.

4.2.2. Estimating the Uncertainties on Derived UV Surface Fluxes

Here we estimate the uncertainties in the UV fluxes estimated from Ca II K using the presented scaling relations (Tables 5 and 6). Important sources of error include the nonsimultaneity of our UV and optical observations, the uncertainties in the Ca II K and UV measurements, the uncertainties in the stellar radii and distances (although the uncertainties in distances for these nearby stars are small) that are used to calculate surface flux, and the uncertainties in the stellar effective temperatures, surface gravities, and metallicities used to calculate the equivalent width correction factors.

Table 5
Fit Parameters for UV Surface Flux and Ca II K Equivalent Width Relations

Transition Name	Wavelength (Å)	log $T_{formation}$[a]	α	β	ρ	n	σ
Si III	1206.50	4.7	1.35 ± 0.26	3.21 ± 0.16	0.80	2.0×10^{-3}	0.59
H I Lyα	1215.67	4.5 (line core)	0.88 ± 0.10	5.46 ± 0.06	0.95	1.1×10^{-5}	0.18
		"active"	1.21 ± 0.16	5.20 ± 0.12	...	...	...
		"inactive"	0.10 ± 0.17	5.19 ± 0.08	...	...	...
Si II	1260.42, 1264.74, 1265.00	4.5	0.99 ± 0.18	2.58 ± 0.11	0.82	6.7×10^{-4}	0.42
C II[b]	1335.71	4.5	1.29 ± 0.23	3.38 ± 0.14	0.82	6.0×10^{-4}	0.54
Mg II[c]	2796.35, 2803.53	4.5 (line core)	1.06 ± 0.13	4.88 ± 0.08	0.94	7.1×10^{-6}	0.27
Si IV	1393.76, 1402.77	4.9	1.35 ± 0.24	3.22 ± 0.14	0.84	3.6×10^{-4}	0.54
He II	1640.4[d]	4.9	1.33 ± 0.15	3.53 ± 0.09	0.91	1.2×10^{-5}	0.41
C IV	1548.19, 1550.78	5.0	1.31 ± 0.26	3.84 ± 0.16	0.81	8.8×10^{-4}	0.56
N V	1238.82, 1242.8060	5.2	1.2 ± 0.26	3.36 ± 0.15	0.77	1.9×10^{-3}	0.55
EUV[e]	100–912	...	0.80 ± 0.09	5.49 ± 0.06	0.94	1.5×10^{-5}	0.18
		"active"	1.37 ± 0.18	5.10 ± 0.14	...	...	...
		"inactive"	0.12 ± 0.18	5.15 ± 0.08	...	...	...

Notes. All relations have the form $\log_{10} F_{S,UV} = (\alpha \times \log_{10} W_{\lambda,corr}) + \beta$, where $F_{S,UV}$ is the surface flux of the UV emission line in erg cm^{-2} s^{-1} and $W_{\lambda,corr}$ is the Ca II K equivalent width in Å. ρ is the Pearson correlation coefficient, n is the probability of no correlation, and σ is the standard deviation of the data points about the best-fit line (dex). The additional fit parameters for Lyα and EUV surface flux apply separately to the "active" ($W_{\lambda,corr} > 1$) and "inactive" M dwarfs ($W_{\lambda,corr} < 1$). Combining the active and inactive fit components, $\sigma = 0.12$ for Lyα, and $\sigma = 0.13$ for the EUV.

[a] Formation temperatures are from the CHIANTI database (Dere et al. 1997; Landi et al. 2013).

[b] Does not include the 1334.54 Å line, due to significant ISM absorption.

[c] Fluxes corrected for 30% ISM absorption (see Section 2.2 and Youngblood et al. 2016).

[d] Average wavelength of the multiplet.

[e] EUV fluxes calculated from Lyα fluxes using scaling relations from Linsky et al. (2014).

The error bars on the $W_{\lambda,corr}$ values come from the dispersion in the many equivalent width measurements made for each target (with the exception of GJ 1132, which has only one measurement), and these error bars range from ~10% to 25%, although Proxima Cen's $W_{\lambda,corr}$ error bar is close to 45%.

Of the nine UV emission lines, Lyα and Mg II have the least scatter about the best-fit line (0.18 and 0.27 dex, respectively). This is important, because these two emission lines compose the majority of the far-UV and near-UV emission line flux, respectively, for the M dwarfs. Considering F(emission line)/$\sum F$(nine emission lines) for the nine stars with measurements for all nine emission lines, F(Lyα)/$\sum F$(nine emission lines) = 65%–91% and F(Mg II)/$\sum F$(nine emission lines) = 6%–27%. The other emission lines compose smaller percentages of the total emission line flux: ~0.1%–5% each. For example, the scatter in the Si III–Ca II K scaling relation is the largest ($\sigma = 0.59$ dex), but F(Si III)/$\sum F$(nine emission lines) = 0.09%–1.7%.

Due to the limited number of EUV observations of M dwarfs, quantifying the true uncertainty in the calculated EUV spectrum is challenging. Here we estimate the uncertainty and list all the main sources of error. Linsky et al. (2014) used *EUVE* observations (100–400 Å) of six M dwarfs with *HST*/STIS Lyα observations, including au Mic, Proxima Cen, AD Leo, EV Lac, and YZ CMi. The 400–912 Å spectra were provided by semiempirical models (Fontenla et al. 2014). Scaling relations for eight ~100 Å bandpasses in the EUV were derived, with dispersions of 13%–24%. Linsky et al. (2014) describe three sources of uncertainty in their technique: errors in the EUV fluxes, errors in the reconstructed Lyα fluxes, and errors associated with stellar variability (the EUV and Lyα observations were not simultaneous). The observed dispersion (13%–24%) in the scaling relations is surprisingly small given the expected magnitudes of the three uncertainty sources. Linsky et al. (2014) attribute this to the avoidance of *EUVE* observations containing flares.

The scatter in our own Ca II K–Lyα relationship is surprisingly small ($\sigma = 0.18$ dex) given the uncertainties listed in the first paragraph of this subsection. The $W_{\lambda,corr}$ error bars range from ~10% to 30%, and Youngblood et al. (2016) find that the uncertainties in the reconstructed Lyα fluxes range from ~5% to 20% for moderate- to high-S/N observations. GJ 1214 was the lowest-S/N observation and had a ~100% uncertainty in the reconstructed flux, but was not included in the Ca II K–Lyα fit.

Starting with a $W_{\lambda,corr}$ measurement with an assumed 30% uncertainty and using the Ca II K–Lyα scaling relation from Table 5, we find that the propagated uncertainty in the calculated Lyα flux is unchanged, indicating that the uncertainty in the Ca II K equivalent width dominates. Using the calculated Lyα flux to estimate the EUV spectrum and adding the 30% uncertainty in quadrature with the 24% dispersion from Linsky et al. (2014) yields an uncertainty of ~40% for the resulting EUV flux.

We have assumed no additional uncertainty due to the variations in metallicity of our target stars. Metallicity variations likely have the largest impact on the H I Lyα–Ca II relations, but it appears that this effect is negligible compared to other sources of scatter for our near-solar-metallicity ($-0.5 \leqslant$ [Fe/H] $\leqslant 0.5$) target stars. The metallicity effect could become significant for metal-poor stars ([Fe/H] < -1), where the relative abundance of Ca with respect to H is approximately an order of magnitude less than for solar-metallicity stars, and we caution against applying these correlations to stars with any physical parameters beyond the bounds of our 15-star sample. The addition of metal-poor M dwarfs into the sample would allow for a determination of the effect of metallicity on these UV–optical correlations.

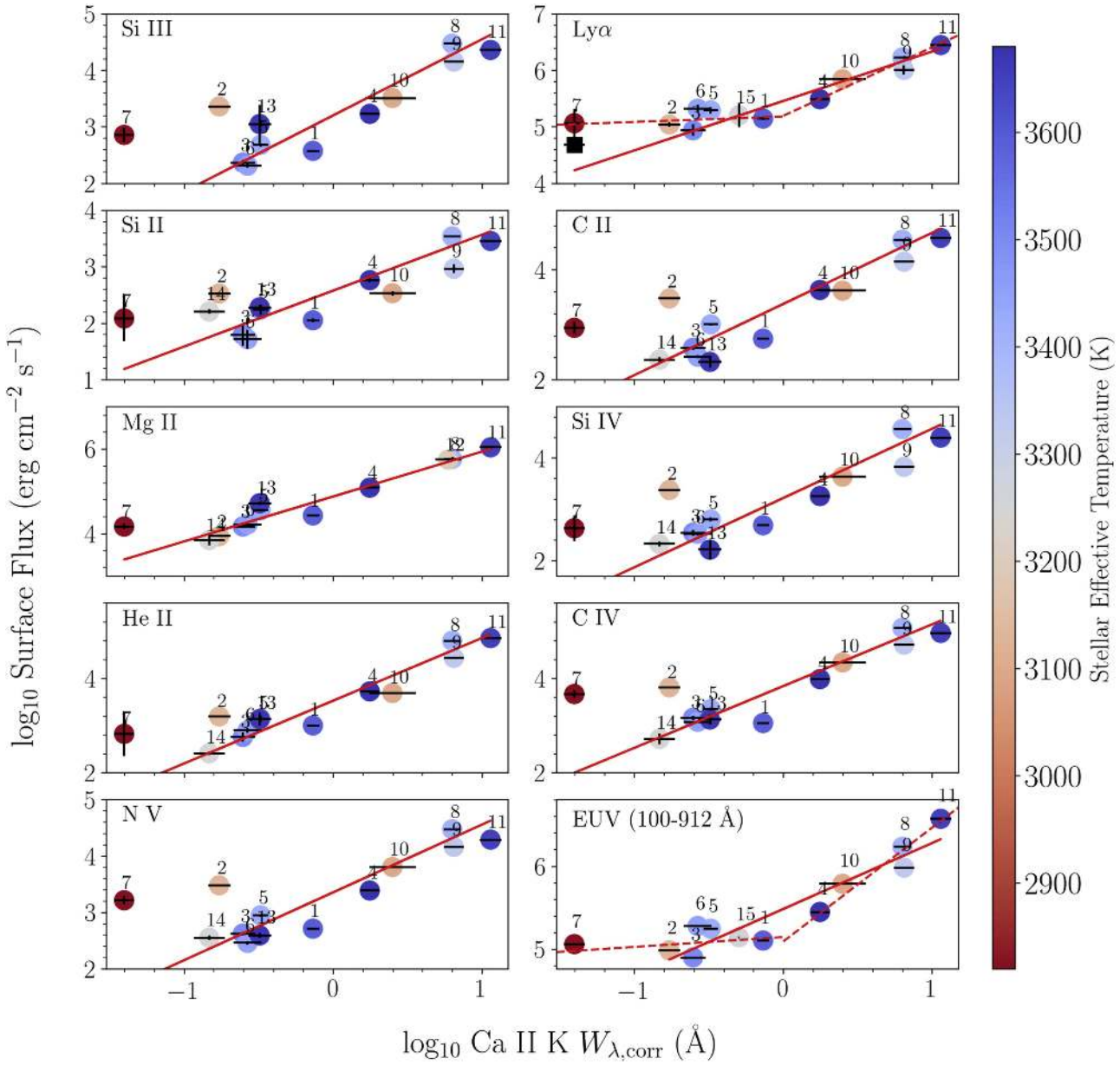

Figure 5. Ca II K (3933 Å) corrected equivalent widths ($W_{\lambda,\mathrm{corr}}$) and surface fluxes for the nine UV emission lines and total EUV flux. Each point represents a different star (numbered to match Table 2) color-coded by effective temperature. In each panel, the solid red line shows a power-law fit to the data. In the Lyα and EUV panels, the dashed red lines show fits applied separately to the "inactive" and "active" M dwarfs. The black square in the top right panel shows the uncorrected Lyα surface flux for GJ 1214 (see Youngblood et al. 2016). GJ 1214 was not included in the Lyα–Ca II K or EUV–Ca II K fits, but was included in all others. The fitted power-law parameters are shown in Table 5.

5. Energetic Proton Estimation from UV Flares

HST has observed dozens of spectrally and temporally resolved far-UV flares from M dwarfs (Loyd & France 2014; France et al. 2016; R. O. P. Loyd et al. 2017, in preparation), which can be used to constrain the time-dependent energy input into the upper atmospheres of orbiting exoplanets. Energetic particles from stellar eruptive events are not frequently included in these energy budgets, because there are no observational constraints for stars other than the Sun. Existing solar correlations between SXRs and protons detected near Earth (i.e., Belov et al. 2007; Cliver et al. 2012) cannot be directly applied to *HST*'s UV flares, because we do not know the energy partition between stellar UV emission lines and SXRs during flares. Thus, we have developed a new scaling relation between energetic protons detected near Earth and UV flares from the Sun.

Ideally, we would determine the relationship between energetic protons detected by the *GOES* satellites and far-UV spectra of the Sun, because this would be directly comparable to the flares detected by *HST*. However, there are no disk-integrated, high-cadence solar observations of UV emission lines within *HST*'s STIS or COS nominal far-UV spectral ranges (1150–1700 Å). We elected to use an EUV emission line from high-cadence solar irradiance measurements as a proxy for far-UV emission lines. *SDO*/EVE measured the solar

Table 6
Formulae for Estimating EUV Fluxes from Lyα and Ca II K

Flux in Wavelength Band at 1 au (erg cm^{-2} s^{-1})	Linsky et al. (2014) Table 4	This Work[a]
F(100–200 Å)	$10^{-0.491} \cdot F(\mathrm{Ly}\alpha)$	$10^{4.97\pm0.06} \cdot W_{\lambda,\mathrm{corr}}^{0.88\pm0.10} \cdot (4.65 \times 10^{-3}\ R_\star)^{2.0}$
F(200–300 Å)	$10^{-0.548} \cdot F(\mathrm{Ly}\alpha)$	$10^{4.91\pm0.06} \cdot W_{\lambda,\mathrm{corr}}^{0.88\pm0.10} \cdot (4.65 \times 10^{-3}\ R_\star)^{2.0}$
F(300–400 Å)	$10^{-0.602} \cdot F(\mathrm{Ly}\alpha)$	$10^{4.86\pm0.06} \cdot W_{\lambda,\mathrm{corr}}^{0.88\pm0.10} \cdot (4.65 \times 10^{-3}\ R_\star)^{2.0}$
F(400–500 Å)	$10^{-2.294} \cdot F(\mathrm{Ly}\alpha)^{1.258}$	$10^{4.57\pm0.08} \cdot W_{\lambda,\mathrm{corr}}^{1.11\pm0.13} \cdot (4.65 \times 10^{-3}\ R_\star)^{2.52}$
F(500–600 Å)	$10^{-2.098} \cdot F(\mathrm{Ly}\alpha)^{1.572}$	$10^{6.49\pm0.09} \cdot W_{\lambda,\mathrm{corr}}^{1.38\pm0.16} \cdot (4.65 \times 10^{-3}\ R_\star)^{3.14}$
F(600–700 Å)	$10^{-1.920} \cdot F(\mathrm{Ly}\alpha)^{1.240}$	$10^{4.85\pm0.07} \cdot W_{\lambda,\mathrm{corr}}^{1.09\pm0.12} \cdot (4.65 \times 10^{-3}\ R_\star)^{2.48}$
F(700–800 Å)	$10^{-1.894} \cdot F(\mathrm{Ly}\alpha)^{1.518}$	$10^{6.39\pm0.09} \cdot W_{\lambda,\mathrm{corr}}^{1.34\pm0.15} \cdot (4.65 \times 10^{-3}\ R_\star)^{3.04}$
F(800–912 Å)	$10^{-1.811} \cdot F(\mathrm{Ly}\alpha)^{1.764}$	$10^{7.82\pm0.11} \cdot W_{\lambda,\mathrm{corr}}^{1.55\pm0.18} \cdot (4.65 \times 10^{-3}\ R_\star)^{3.53}$

Note. $F(\mathrm{Ly}\alpha)$ is the Lyα flux at 1 au (erg cm^{-2} s^{-1}), and $W_{\lambda,\mathrm{corr}}$ is the Ca II K corrected equivalent width (Equation (2)).
[a] Substituted Lyα–$W_{\lambda,\mathrm{corr}}$ scaling relation from Table 5 into the relation from Linsky et al. (2014); $R_\star$ in units of $R_\odot$; uncertainties propagated from fit uncertainties in Table 5.

spectral irradiance of the Sun from 50 to 370 Å in the MEGS-A channel at 10 s cadence from 2010 to 2014. The only high-S/N ion with a formation temperature similar to those accessible by *HST* STIS/COS in the far-UV is He II at 304 Å (log $T_{\mathrm{formation}} = 4.9$; CHIANTI; Dere et al. 1997; Landi et al. 2013). The far-UV flare tracers Si IV (1393, 1402 Å; log $T_{\mathrm{formation}} = 4.9$) and He II (1640 Å; log $T_{\mathrm{formation}} = 4.9$) observed by *HST* have similar formation temperatures to He II λ304. After determining the relationship between >10 MeV proton flux and He II λ304, we use the semiempirical model of GJ 832 (M1.5 V; Fontenla et al. 2016) to scale He II λ304 flux to Si IV and He II λ1640 flux. In Section 5.4, we estimate the proton flux from an Si IV flare observed with *HST* from the M4 dwarf GJ 876, and in Section 5.5, we discuss the limitations of applying these proton scaling relationships to flares on M dwarfs.

5.1. The Solar Flare and Proton Enhancement Sample

We identified 36 proton enhancements in the *GOES* >10 MeV and >30 MeV proton channels with an associated SXR (1–8 Å with *GOES*) and He II λ304 flare. Our confidence levels for the proton–flare association varied, and we assigned each event a quality index (q) ranging from 1 (lowest confidence) to 4 (highest confidence). The number of events assigned to $q = 1$, 2, 3, and 4 is 7, 11, 7, and 11, respectively. Reasons for a low q include difficulty in identifying a proton enhancement's precursor flare and/or reliably measuring the properties of both fluxes. There can be too many candidate precursor flares, low S/N, difficulty in defining the beginning and end of the proton and flare events, and uncertainty in measuring background flux level. Figure 6 shows an example high-confidence event ($q = 4$) and a low-confidence event ($q = 1$). For the $q = 1$ example event, the onset of the >10 MeV protons after the photon flares is much more gradual than most events, and the >30 MeV proton flux shows no significant rise. The He II λ304 light curve also shows many events, which may be confused, and estimation of the background level is challenging.

We find that the proton, UV, and SXR flux errors are dominated by systematics in defining a background flux level to subtract and the duration of the flare. We applied a linear fit to the background around each event. For some events, this was straightforward, but for others, this method likely increases uncertainty in the measurement. We determined the beginning and end of the flare by where the light curve intersected the background level fit. To estimate the uncertainties in our measurements, we remeasured 4 of the 36 events three times, each time slightly changing the background fit and the beginning and end of the flare. We estimate the uncertainty in the background-subtracted flux to range from 10% to 300% for SXR, 10%–200% for He II λ304, and 10%–30% for the protons. These ranges are a reflection of the varying quality factors: $q < 3$ events have the largest uncertainties, and $q \geqslant 3$ events have the smallest uncertainties. If we consider just the fluence (no background subtraction) or the peak fluxes, the uncertainties drop to 10% for the SXRs and He II λ304, indicating that background subtraction and not flare duration is the dominant uncertainty.

The 36 He II λ304 flares have mean durations 5.3 ± 4.6 hr and on average peak a few minutes after the SXR flare peak, although there is large scatter in this average. When examining only the $q \geqslant 3$ events, the average He II λ304 peak occurs ~5 minutes before the SXR peak. Kennedy et al. (2013) used He II λ304 to trace the impulsive phase flares and found He II λ304 to peak 1–4 minutes before the SXR peak, which traces the more gradual phase of the flare, and Milligan et al. (2012) found for an X-class flare that He II λ304 peaked 18 s before the *GOES* SXRs. The associated proton enhancements begin within about 2 hr of the SXR peak and on average last for 3 days. Part of the scatter in the He II λ304–proton relationships presented in Figure 7 is due to overlapping flares with contributing protons. In the duration of a proton enhancement, the same or another active region could flare again and accelerate protons that reach Earth. Many of the >10 MeV enhancements have many peaks over the course of several days, while the >30 MeV enhancements typically only have a rapid initial peak and a gradual decline. The peak proton fluxes between the two channels generally do not coincide temporally; the >10 MeV peak particle flux typically occurs after the >30 MeV peak. The energy-dependent arrival times of protons are not completely explained by differing speeds; it is thought that higher-energy protons are accelerated with electrons close to the solar surface and that either lower-energy protons are accelerated at a later time (farther from the solar surface) or their escape from the Sun is delayed owing to trapping by shocks (Krucker & Lin 2000; Xie et al. 2016).

In their sample of 58 SXR and proton enhancement events, Cliver et al. (2012) found a statistically significant correlation ($\rho = 0.52$, $n = 3 \times 10^{-5}$), but our 36-event sample yields

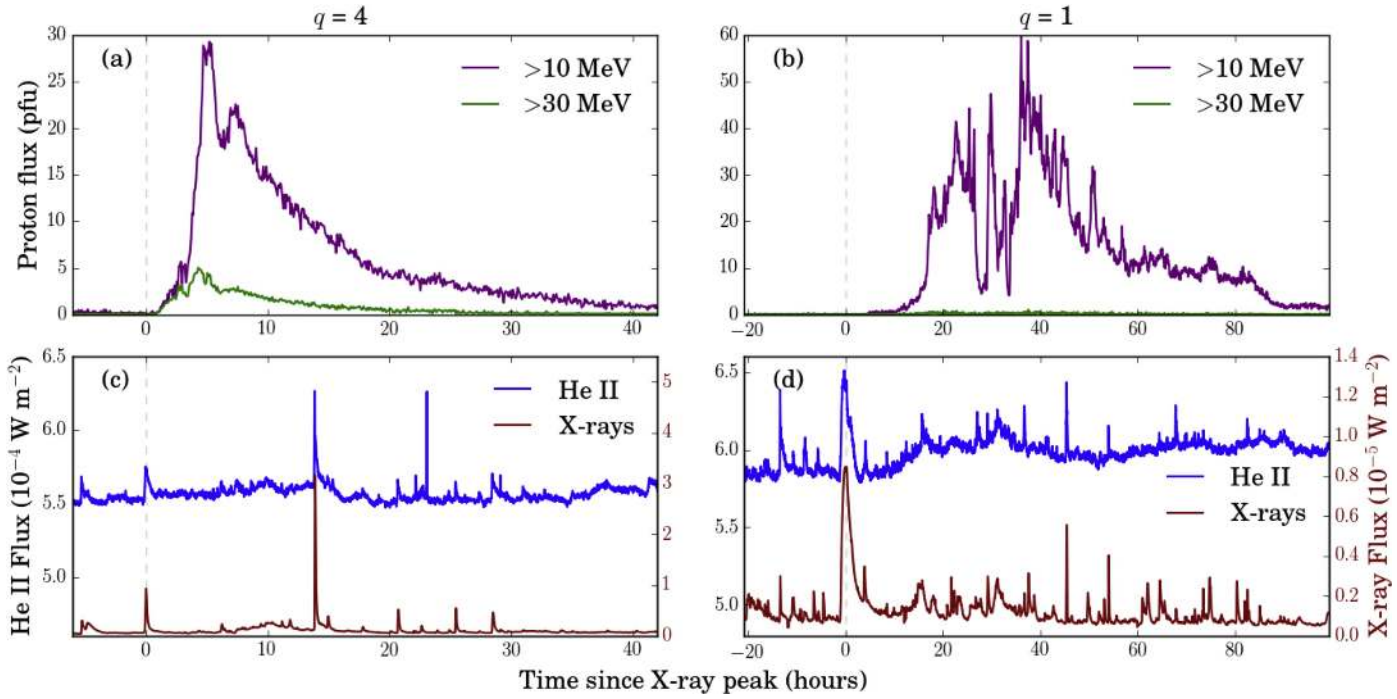

Figure 6. Examples of SXR and He II (304 Å) flares and corresponding proton enhancements. Panels (a) and (c) show an example where we have high confidence ($q = 4$) in the He II λ304 flux measurement and that the events are associated. This SXR flare peaked on 2013 December 12 18:02:35 UTC. Panels (b) and (d) show an example event where we have low confidence ($q = 1$) in both the measured He II λ304 flux and the association between the flare and proton enhancement. This SXR flare peaked on 2012 August 31 20:44:05 UTC.

$\rho = 0.18$, $n = 0.3$ (Figure 8). If we force both samples to cover the same parameter space (enclosed in the vertical lines in Figure 8), the correlation coefficients become similar: $\rho = 0.41$, $n = 0.003$ for 50 of Cliver et al. (2012) events, and $\rho = 0.35$, $n = 0.05$ for 33 of our events. The different n values are due to the different sample sizes.

5.2. Solar UV–Proton Scaling Relations

We observe statistically significant correlations between He II λ304 fluence (time-integrated flux with units J m^{-2}) and proton fluence and peak proton flux (all fluence and flux values background subtracted; Figure 7). The data were fitted with power laws ($\log_{10} x = \alpha \times \log_{10} y + \beta$), and the parameters for the fits are presented in Table 7. The scatter in these fits is large ($\sigma = 0.75$–0.84 dex).

The near identical formation temperatures of He II λ304, Si IV, and He II λ1640 suggest that the ratios of their fluxes are likely to be similar for all stars with metallicities similar to solar values. Thus, we estimated these ratios using synthetic spectra of the Sun (CHIANTI; Dere et al. 1997; Landi et al. 2013) and GJ 832 (Fontenla et al. 2016). For the Sun, $F_{\mathrm{Si\,IV}}/F_{\mathrm{He\,II,304}} = 0.117$ and $F_{\mathrm{He\,II,1640}}/F_{\mathrm{He\,II,304}} = 0.0304$. For GJ 832, $F_{\mathrm{Si\,IV}}/F_{\mathrm{He\,II,304}} = 0.137$ and $F_{\mathrm{He\,II,1640}}/F_{\mathrm{He\,II,304}} = 0.0291$. The ratios for these two stars are very similar, so we will use the GJ 832 ratios in the subsequent analysis. However, we note that the ratios could change by a factor of a few during a flare as estimated by comparing flux ratios of various lines for the active and quiet-Sun models listed in Table 1 of Fontenla et al. (2016). More M dwarf atmosphere models calculated at a range of activity levels would be valuable.

We apply the quiescence ratios to our proton–He II λ304 relations (Table 7) to relate Si IV and He II λ1640 flare flux to proton enhancements. Using one of the correlations listed in Table 7 and replacing $F_{\mathrm{He\,II,304}}$ with $F_{\mathrm{Si\,IV}}$, we find that

$$\log I_{>10\mathrm{MeV}} = (1.06 \pm 0.21) \times \log F_{\mathrm{Si\,IV}} + (3.34 \pm 0.25), \quad (3)$$

where $F_{\mathrm{Si\,IV}}$ is the background-subtracted Si IV ($\lambda\lambda$1393, 1402) flare fluence (J m^{-2}) as would be observed at 1 au from the star, and $I_{>10\mathrm{MeV}}$ is the background-subtracted peak >10 MeV proton enhancement intensity (pfu; 1 pfu = 1 proton cm^{-2} s^{-1} sr^{-1}) as would also be observed at 1 au. If instead the proton fluence ($F_{>10\mathrm{MeV}}$, [pfu · s]) rather than peak proton flux is used, the relationship becomes

$$\log F_{>10\mathrm{MeV}} = (1.20 \pm 0.26) \times \log F_{\mathrm{Si\,IV}} + (3.27 \pm 0.31). \quad (4)$$

Similarly, we can derive $I_{\geqslant 10\mathrm{MeV}}$ and $F_{\geqslant 10\mathrm{MeV}}$ from $F_{\mathrm{He\,II,1640}}$:

$$\log I_{>10\mathrm{MeV}} = (1.06 \pm 0.21) \times \log F_{\mathrm{He\,II,1640}} + (4.05 \pm 0.36), \quad (5)$$

and

$$\log F_{>10\mathrm{MeV}} = (1.20 \pm 0.26) \times \log F_{\mathrm{He\,II,1640}} + (4.07 \pm 0.45). \quad (6)$$

5.3. UV-based GOES Flare Classification

When using Equations (3)–(6), it is important to note that not all far-UV flares will be accompanied by particle events. Less energetic flares are less likely to produce particles. The solar relation was quantified by Yashiro et al. (2006) using the *GOES* SXR classification scheme as the metric of flare strength. Specifically, they associated a probability of a CME with each *GOES* flare class. To relate this to far-UV data,

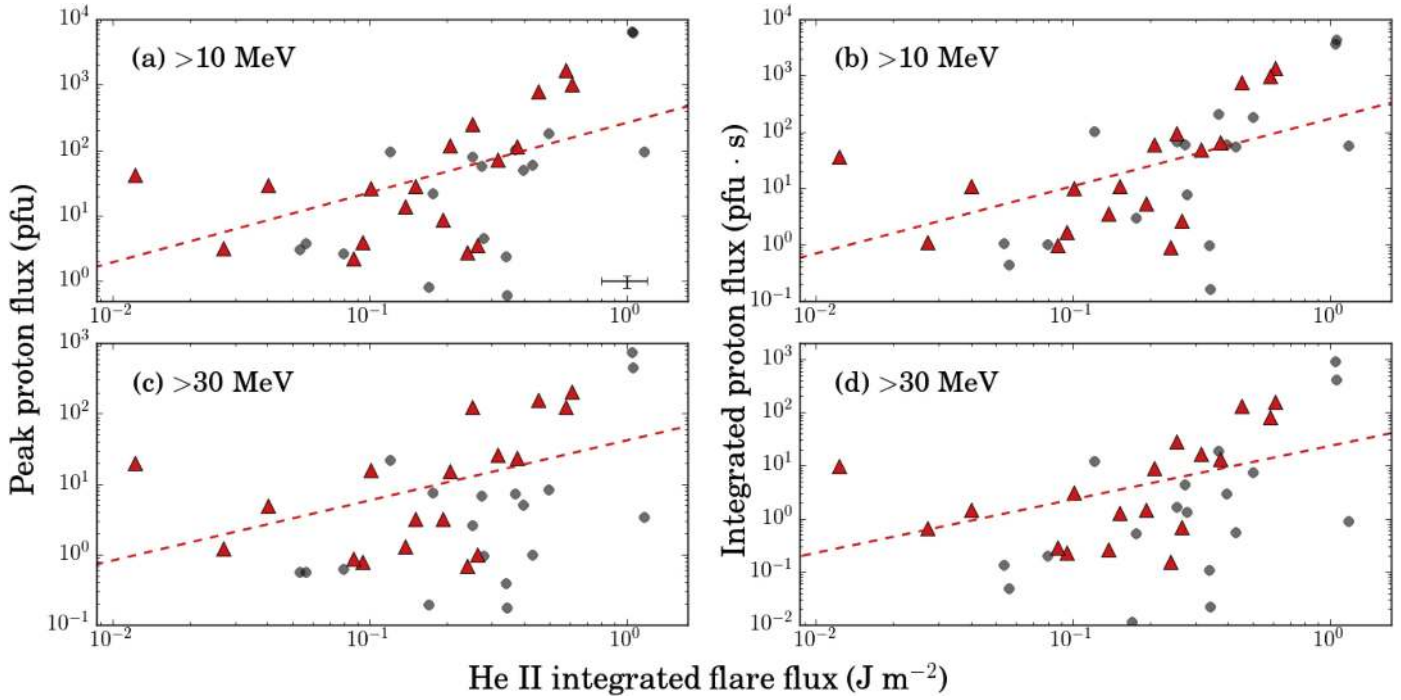

Figure 7. Relations between background-subtracted He II (304 Å) flare fluence and peak flux and fluence of likely associated proton enhancements. The red triangles represent data points with a quality factor $q \geqslant 3$, and the dashed red lines show power-law fits to those points. The gray circles represent the data points $q \leqslant 2$ and were excluded from the fits. Panels (a) and (c) show the peak proton flux (background subtracted), and (b) and (d) show the proton fluence (background subtracted). 1 pfu = 1 proton cm^{-2} s^{-1} sr^{-1}. The fit parameters are listed in Table 7, and representative 20% error bars for the $q > 3$ data points are shown in the lower right corner of panel (a).

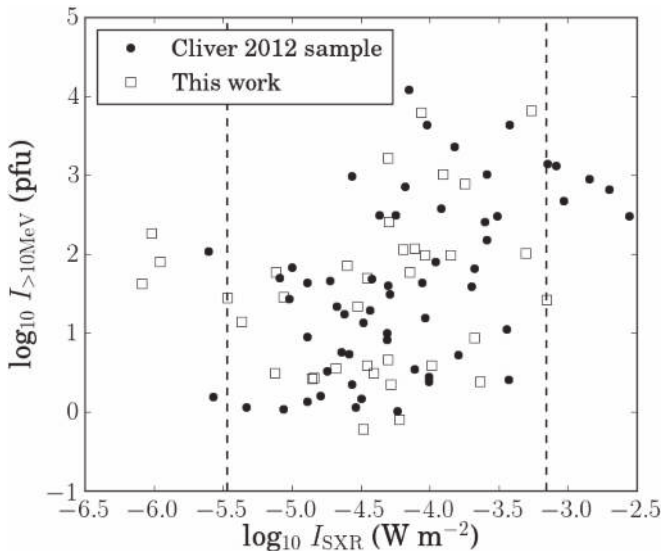

Figure 8. SXR (1–8 Å) peak flare intensity (not background subtracted per *GOES* standards; I_{SXR}; W m^{-2}) and peak >10 MeV proton flux ($I_{>10\mathrm{MeV}}$; pfu). Filled black circles show the 58 events presented in Figure 2 of Cliver et al. (2012), and the open black squares show the 36 events presented in this work. The two vertical dashed lines enclose the data points that cover the same SXR parameter range.

we used our 36 events to fit an empirical power law between peak SXR intensity and peak He II λ304 intensity (W m^{-2}; Figure 9):

$$\log I_{\mathrm{SXR}} = (1.40 \pm 0.09) \times \log I_{\mathrm{He\,II,304}} + (1.52 \pm 1.62). \quad (7)$$

The Pearson correlation coefficient is 0.58 with $n = 2.2 \times 10^{-4}$ for the 36 events used in this analysis. The scatter about the best-fit line in Figure 9 is 0.52 dex, so the resulting classifications for M dwarf flares will be accurate within a factor of a few. This level of accuracy will be problematic for small flares (<X class), but less so for large flares, due to the ~100% chance of associated proton enhancement (Table 1). Using our conversion ratio ($F_{\mathrm{Si\,IV}}/F_{\mathrm{He\,II,304}} = 0.137$) and assuming $F_{\mathrm{Si\,IV}}/F_{\mathrm{He\,II,304}} \sim I_{\mathrm{Si\,IV}}/I_{\mathrm{He\,II,304}}$, we can estimate the peak SXR flux from the peak Si IV and He II λ1640 flux:

$$\log I_{\mathrm{SXR}} = (1.4 \pm 0.1) \times \log I_{\mathrm{Si\,IV}} + (2.7 \pm 1.6), \quad (8)$$

and

$$\log I_{\mathrm{SXR}} = (1.4 \pm 0.1) \times \log I_{\mathrm{He\,II,1640}} + (3.7 \pm 1.6). \quad (9)$$

Approximately 20% of C-class flares ($F_{\mathrm{SXR}} = 10^{-6}$–$10^{-5}$ W m^{-2} at 1 au) and ~100% of X3-class or greater flares ($F_{\mathrm{SXR}} \geqslant 3 \times 10^{-4}$ W m^{-2} at 1 au) have associated CMEs (Yashiro et al. 2006; Table 1). Recall that F_{SXR} is the peak 1–8 Å flare intensity measured at 1 au from the star and is not corrected for pre-flare flux levels. An X-class or greater flare ($\geqslant 10^{-4}$ W m^{-2} at 1 au) corresponds to any Si IV flare with a background-subtracted peak intensity value $\geqslant 1.6 \times 10^{-5}$ W m^{-2} = 1.6×10^{-2} erg cm^{-2} s^{-1} at 1 au and to any He II λ1640 flare with a background-subtracted peak intensity value $\geqslant 3.2 \times 10^{-6}$ W m^{-2} = 3.2×10^{-3} erg cm^{-2} s^{-1} at 1 au.

5.4. Application to Observed Flares from GJ 876

The MUSCLES Treasury Survey observed several large flares from GJ 876 ($d = 4.7$ pc) with *HST* and *Chandra* in 2015

Table 7
Correlations between UV Flare Fluence (F) and the Peak Intensity (I) and Fluence (F) of Energetic Protons during Solar Flares

x	y	α	β	ρ	n	σ
$F_{\text{He II},304}$	$I_{\geqslant 10\text{MeV}}$	1.06 ± 0.21	2.42 ± 0.17	0.83	2.2×10^{-5}	0.76
$F_{\text{He II},304}$	$I_{\geqslant 30\text{MeV}}$	0.85 ± 0.20	1.62 ± 0.16	0.80	6.5×10^{-5}	0.75
$F_{\text{He II},304}$	$F_{\geqslant 10\text{MeV}}$	1.20 ± 0.26	2.23 ± 0.21	0.84	1.0×10^{-5}	0.84
$F_{\text{He II},304}$	$F_{\geqslant 30\text{MeV}}$	1.01 ± 0.25	1.37 ± 0.20	0.82	3.6×10^{-5}	0.84
$F_{\text{Si IV}}$	$I_{\geqslant 10\text{MeV}}$	1.06 ± 0.21	3.34 ± 0.25	⋯	⋯	⋯
$F_{\text{Si IV}}$	$F_{\geqslant 10\text{MeV}}$	1.20 ± 0.26	3.27 ± 0.31	⋯	⋯	⋯
$F_{\text{He II},1640}$	$I_{\geqslant 10\text{MeV}}$	1.06 ± 0.21	4.05 ± 0.36	⋯	⋯	⋯
$F_{\text{He II},1640}$	$F_{\geqslant 10\text{MeV}}$	1.20 ± 0.26	4.07 ± 0.45	⋯	⋯	⋯

Note. The power-law fits ($\log_{10} x = \alpha \times \log_{10} y + \beta$) are based on the $q \geqslant 3$ background-subtracted data (Figure 7). ρ is the Pearson correlation coefficient, n is the probability of no correlation, and σ is the standard deviation of the data points about the best-fit line (dex).

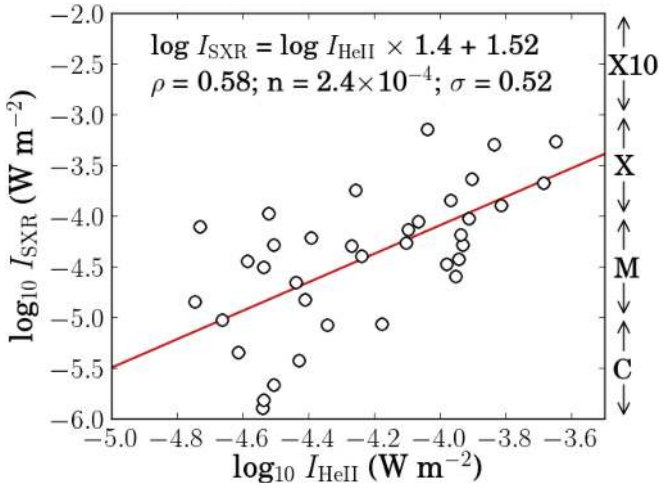

Figure 9. He II λ304 peak flare intensity (background subtracted; $I_{\text{He II}}$) and SXR (1–8 Å) peak flare intensity (not background subtracted per *GOES* standards; I_{SXR}) of the 36 events (circles). The right side of the plot is marked with the *GOES* SXR flare classification scheme, which is also described in Table 1.

June and July (France et al. 2016; R. O. P. Loyd et al. 2017, in preparation; Figure 10). Due to an *HST* safing event, the *Chandra* and *HST* observations were not simultaneous as originally planned. On 2015 June 5, the SXR luminosity of GJ 876 was observed to increase by a factor >10 (Figure 10(a)), and on 2015 July 7, factor of ∼40–100 increases were observed in the far-UV lines, including Si IV (Figure 10(b)), and more modest increases (factor of ∼5) were observed in the far-UV continuum (France et al. 2016). He II λ1640 was observed with a different grating than Si IV, so the two emission lines were not observed simultaneously, and no clear flare was observed in He II λ1640 on 2015 July 8 (Figure 10(c)), although the C IV light curve indicates that GJ 876 did flare during this observation. In this section and Table 8, we characterize the magnitude of these flares with the *GOES* flare classification scheme and estimate the probability and magnitude of an associated particle enhancement received in GJ 876's HZ ($\langle r_{\text{HZ}} \rangle = 0.18$ au; Kopparapu et al. 2014). See Section 5.5 for a discussion on the limitations of these results.

Table 1 provides comparison points for solar flares, and in Table 8 we note the *GOES* classification and other parameters for well-known solar and stellar flares to give context for the GJ 876 flares. The Carrington event of 1859, arguably the largest solar flare ever recorded, has been calculated to be an X45 (±5) class flare (Cliver & Dietrich 2013). The November 4 solar flare of the Halloween storms in 2003, probably the largest flare observed during the space age, is estimated to be an X30.6-class flare (Kiplinger & Garcia 2004; note that the *GOES* detectors saturate for events between X10 and X20). For the great AD Leo flare of 1985 (Hawley & Pettersen 1991), Segura et al. (2010) estimated that an HZ planet ($\langle r_{\text{HZ}} \rangle = 0.16$ au) would have received peak >10 MeV proton and SXR fluxes of 5.9×10^8 pfu and 9 W m^{-2}, respectively. The peak SXR flux at 1 au (0.23 W m^{-2}) would make this an X2300-class flare. Osten et al. (2016) found that the superflare observed from the young M dwarf binary system DG CVn was equivalent to an X600,000-class flare (60 W m^{-2} at 1 au, or 6000 W m^{-2} at 0.1 au, the approximate HZ distance). We note, however, that there is evidence that SXR–proton scaling relations should break down for such large events (>X10-class; Hudson 2007; Drake et al. 2013).

We measure the peak flux for the large GJ 876 SXR flare observed at ∼45 ks in Figure 10(a) to be $(9.72 \pm 1.28) \times 10^{-13}$ erg cm^{-2} s^{-1} in the 0.3–10 keV bandpass (1.25–41 Å). A total of 11% ± 1.3% of the flare flux was emitted at energies 1.5–10 keV (1.25–8 Å), similar to the *GOES* long channel (1–8 Å), so we find that this flare is equivalent to an M9.5-class flare (error range: M7.8–X1.1; Table 1). X1-class flares have an 80%–100% chance of associated energetic particles from the Sun (Yashiro et al. 2006), with an estimated peak proton flux of ∼80 pfu at 1 au (Cliver et al. 2012). The SXR and proton fluxes received in GJ 876's HZ will be ∼30 × larger: 2.8×10^{-3} W m^{-2} and 2400 pfu, respectively. Veronig et al. (2002) find that the Sun emits X-class flares roughly every month, but flares that unleash SXR fluxes of 10^{-3} W m^{-2} on Earth occur only approximately once every 5 yr.

The smaller GJ 876 SXR flare observed at ∼7 ks in Figure 10(a) is estimated to be equivalent to an M2.2-class flare (Table 1). This smaller flare has a 40%–80% chance of associated energetic particles (Yashiro et al. 2006) with an estimated peak proton flux of ∼8 pfu at 1 au. M-class flares are emitted by the Sun about every other day (Veronig et al. 2002), but flares that are a factor of 30 larger in SXR and proton fluxes, as would be experienced in GJ 876's HZ, occur only a few times per year.

GJ 876's 10^{31} erg UV flare ($\Delta\lambda = 400$–1700 Å) observed on 2015 July 7 with *HST* (France et al. 2016) emitted 1.2×10^{29} erg in the Si IV emission line over ∼25 minutes

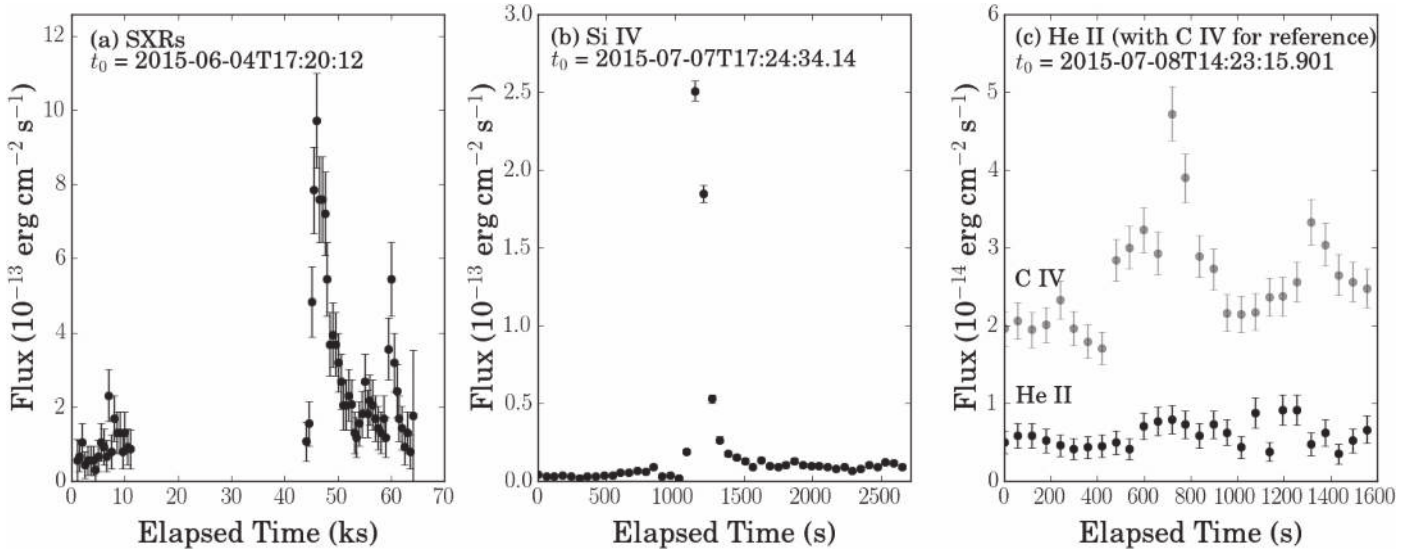

Figure 10. Sample of observed GJ 876 flares. (a) *Chandra*/ACIS-S3 SXR light curve (1.55–10.0 keV) in 500 s time bins presented originally in France et al. (2016). (b) *HST*/COS Si IV light curve in 60 s time bins. (c) *HST*/COS He II λ1640 light curve (black filled circles) in 60 s time bins. The C IV light curve (gray filled circles) is shown to reference when a flare occurred.

(Figure 10(b)). Using Equation (3) and the fluence at 1 au, we find that the peak proton flux received at 1 au during the flare was ~75 pfu, or ~2300 pfu at 0.18 au. Using the SXR–UV scaling relation (Equation (8)) and the observed Si IV flare peak, we find that this flare was X38-class with an estimated error of a factor of ~3 (X13–X114). Note that the peak proton flux calculated for this 2015 July 7 Si IV flare (~2300 pfu at 0.18 au) is similar to the peak proton flux calculated for the 2015 June 5 SXR flare (~2400 pfu at 0.18 au), but that the *GOES* classifications are different: M9.5 compared to X38, or a factor of 40 difference in SXR flux.

In total, *Chandra* observed three M- to X-class flares in 8.25 hr, and *HST* observed six comparable flares (within an order of magnitude) in 12.35 hr, including observations from the MUSCLES pilot survey (France et al. 2013). Thus, we estimate that GJ 876 emits flares of this magnitude at a rate of ~0.4–0.5 hr^{-1}. From Veronig et al. (2002), the Sun's rate of M-class flares is ~0.02 hr^{-1}, a factor of ~20 less frequent than GJ 876. However, note that these M-class flares are effectively 30× stronger (i.e., X10-class) in GJ 876's HZ at 0.18 au. The Sun emits X10-class flares approximately once every 5 yr, so planets in the GJ 876 HZ are receiving SXR flare fluxes $\geqslant 10^{-3}$ W m^{-2} associated with proton fluxes ~10^3 pfu about four orders of magnitude more frequently than Earth.

In Figure 11, we show the effect of frequent X-class flares with associated proton enhancements on the O_3 column depth in an Earth-like atmosphere with no magnetosphere (Segura et al. 2010; M. A. Tilley et al. 2017, in preparation). For comparison to the M- to X-class GJ 876 flares analyzed in this section, we show the dramatic responses of O_3 after the great AD Leo flare (Segura et al. 2010) and the Carrington event (see Table 8). To represent the GJ 876 flares discussed in this section, we scaled the SED of the great AD Leo flare (Hawley & Pettersen 1991) down in intensity and duration to match flares of the dM4e star GJ 1243 (Hawley et al. 2014). This resulted in ~X1-class flares with ~4-minute durations. Peak proton fluxes were assigned as 1.2×10^3 pfu (a typical value for the flares discussed in this section), and we provide two cases distinguished by their flare frequency: 0.08 hr^{-1} (Case A) and 0.5 hr^{-1} (Case B; similar to GJ 876's observed flare frequency). Both the Case A and Case B flares turn off after a period of 40 months, but via extrapolation, we show that for Case A, the O_3 column approaches near-complete depletion at approximately 10^{13} s (318 kyr) of similar, constant stellar activity. Case B shows near-complete O_3 depletion after only approximately 5×10^9 s (160 yr). Given the several-gigayear period of high activity during the evolution of early to mid-M dwarfs, both scenarios indicate massive, and likely complete, O_3 depletion. This suggests that planetary surfaces in the HZ would be bathed in stellar UV flux. A detailed analysis of atmospheric effects will be presented in the upcoming work by M. A. Tilley et al. (2017, in preparation).

5.5. Limitations of the Method

Our new method of proton flux estimation due to stellar flares has important limitations, but it will be useful until advancements are made in the indirect detection of particles from stellar eruptive events (e.g., coronal dimming or Type II or III radio bursts; Crosley et al. 2016; Harra et al. 2016) or in our understanding of particle acceleration under kilogauss magnetic field strengths. The scaling relations are statistical and are relatively inaccurate for individual flares.

The first caveat to the method is that we are necessarily assuming that particle acceleration in M dwarf atmospheres is similar to that in the Sun. This could be a poor assumption as M dwarfs have different atmospheric structure and stronger surface magnetic fields. Magnetic processes are ultimately responsible for flares and particle acceleration. Also, fast-rotating M dwarfs have extremely large surface magnetic fields with photospheres possibly saturated with active regions. Overlying magnetic fields could prevent the acceleration of particles away from the stellar atmosphere (e.g., Vidotto et al. 2016). This phenomenon was observed on the Sun in 2014 October when the large active region 2192 emitted many X-class flares, which have a >90% probability of an associated CME, but no CMEs were ejected. Strong overlying magnetic

Table 8
GJ 876 Flare Properties

Flare	Peak SXR Flux (W m^{-2})		*GOES* Class	>10 MeV Proton Flux (pfu)	
	1 au	$\langle r_{HZ} \rangle$		1 au	$\langle r_{HZ} \rangle$
GJ 876 flares:					
2015 Jun 4	2.2×10^{-5}	6.6×10^{-4}	M2.2	8	240
2015 Jun 5	9.5×10^{-5}	2.9×10^{-3}	M9.5	80	2400
2015 Jul 7	3.8×10^{-3}	1.1×10^{-1}	X38	75	2300
Reference flares:					
Carrington Event 1859[a]	4.5×10^{-3}	...	X45 ± 5	...	...
2003 Nov 4 solar flare[b]	3.06×10^{-3}	...	X30.6	400	...
Great AD Leo flare of 1985[c]	0.23	9	X2300	1.5×10^{6}	5.9×10^{8}
DG CVn 2014 Apr 24[d]	60	6000	X600,000	...	...

Note. $\langle r_{HZ} \rangle$ = 0.18 au for GJ 876; 0.16 au for AD Leo; 0.1 au for DG CVn; 1 au for the Sun.
Reference. (a) Cliver & Dietrich (2013), (b) Kiplinger & Garcia (2004), (c) Segura et al. (2010), (d) Osten et al. (2016).

fields were observed and have been cited as a possible explanation for the lack of associated CMEs (Sun et al. 2015; Thalmann et al. 2015).

We should be careful when extrapolating solar-based SXR–particle scaling relations to large energies. There is evidence for a break in the SXR–proton power law around X10-class flares (see Lingenfelter & Hudson 1980; Hudson 2007, and references therein). It is unclear whether only the expected proton flux flattens out for increasingly large SXR flares (>X10), or whether the frequency of >X10-class flares also breaks from the expected power-law frequency distribution (e.g., Veronig et al. 2002). This uncertainty is partly due to the rarity of these energetic events, but also because the *GOES* SXR detectors saturate around 10^{-3} W m^{-2}. Drake et al. (2013) find that extrapolating SXR–CME scaling relations to energies applicable to highly active solar-type stars would require CMEs to account for ~10% of the total stellar luminosity, a likely unreasonable fraction. Those authors conclude that the SXR–CME scaling relations must flatten out at some point.

Predicting proton flux even for the Sun is not an easy feat, because the mechanisms of particle acceleration are not well understood. SXRs and UV photons during flares correlate with particle flux, and Kahler (1982) proposes that such correlations are manifestations of "Big Flare Syndrome," which describes how the energy of an eruptive event can power numerous physical processes that are not directly linked. Thermally heated plasma ($T > 80{,}000$ K) emits short-wavelength photons that we observe as a flare, but particles are accelerated by a nonthermal process, and the ambient corona is thought to be the major contributor to CME mass (Sciambi et al. 1977; Hovestadt et al. 1981). For our purposes of estimating proton fluxes from M dwarfs and their effects on orbiting planets, a correlation between photons and particles without direct causation is valuable.

Another limitation is our use of the GJ 832 synthetic spectrum from Fontenla et al. (2016) to estimate He II λ304 flare flux from far-UV Si IV or He II λ1640 flare flux. The model is applicable to the quiescent star, and flux ratios between emission lines likely change during a flare. Comparing flux ratios between the active and quiet-Sun models listed in Table 1 of Fontenla et al. (2016), the ratios of emission lines formed at different temperature change by a factor of a few during a flare. In a future work, we will improve the flux ratio relations using flare atmospheres.

We chose He II λ304 as a proxy because of its similar formation temperature to Si IV λλ1393,1402 (and He II λ1640), but we note that the electrons responsible for the collisional excitation of He II λ304 (40.8 eV above ground) must have significantly higher energies than the thermal electrons at $T_{form} = 80{,}000$ K ($k_B T_{form} = 6.9$ eV) that collisionally excite Si IV (8.8 eV above ground; Jordan 1975). Higher-energy electrons could diffuse down through the transition region, as recombination/ionization timescales are much longer than dynamical timescales (e.g., Shine et al. 1975; Golding et al. 2014, 2016). Also, the He II line fluxes receive some contribution from recombination, and this becomes more important during flares.

Another challenge in the analysis is quantifying the probability that any ejected particles will intersect the exoplanet. There are many unknowns here, including the interplanetary magnetic field topology that charged particle trajectories will follow (Parker 1958); the opening angle of the accelerated particles; the planet's cross section, which may be larger than πR_p^2 owing to the presence of a magnetosphere; and the direction of the particle ejection with respect to the planet's orbital plane (see Kay et al. 2016). A thorough treatment of this issue is beyond the scope of this work.

6. Summary

In this paper, we have developed methods for estimating the high-energy radiation and particle environments of M dwarfs for use when direct observations are unavailable. We have empirically determined scaling relations that can be used to estimate the UV spectra of M dwarfs from optical spectra and the energetic particle flux from UV flares. The main results of this work are summarized as follows.

Table 9
UV–UV Emission Line Scaling Relations

UV1, UV2	m	σ_m	b	σ_b	ρ	n	σ
Lyα, Si III	0.60	0.09	3.66	0.35	0.89	6.4E–04	0.23
Si II, Si III	0.82	0.04	−0.11	0.18	0.97	2.3E–07	0.15
C II, Si III	1.01	0.07	0.13	0.30	0.94	8.1E–06	0.27
Mg II, Si III	0.79	0.35	2.26	1.11	0.84	2.2E–03	0.36
Si IV, Si III	1.01	0.04	−0.01	0.16	0.92	1.7E–05	0.29
He II, Si III	1.15	0.14	−0.2	0.6	0.95	1.6E–06	0.26
C IV, Si III	1.03	0.04	0.49	0.19	0.96	7.5E–07	0.21
N V, Si III	0.87	0.04	0.52	0.18	0.96	1.0E–06	0.20
Si II, Lyα	1.16	0.21	−3.83	1.29	0.87	1.1E–03	0.30
C II, Lyα	1.71	0.27	−6.26	1.60	0.88	7.4E–04	0.40
Mg II, Lyα	1.38	0.15	−2.68	0.84	0.96	1.1E–04	0.19
Si IV, Lyα	1.71	0.25	−6.27	1.47	0.90	4.1E–04	0.38
He II, Lyα	1.91	0.29	−7.26	1.71	0.96	1.6E–05	0.32
C IV, Lyα	1.58	0.19	−4.86	1.15	0.92	2.0E–04	0.32
N V, Lyα	1.43	0.21	−4.58	1.25	0.88	9.1E–04	0.35
C II, Si II	1.33	0.11	−0.05	0.38	0.93	4.1E–06	0.28
Mg II, Si II	1.57	0.27	0.54	0.78	0.86	6.0E–04	0.47
Si IV, Si II	1.31	0.09	−0.12	0.30	0.92	1.1E–05	0.30
He II, Si II	1.57	0.14	−0.59	0.49	0.93	3.7E–06	0.32
C IV, Si II	1.3	0.08	0.47	0.28	0.9	2.4E–05	0.33
N V, Si II	1.18	0.10	0.23	0.36	0.92	1.0E–05	0.27
Mg II, C II	0.75	0.25	2.23	0.84	0.83	1.7E–03	0.39
Si IV, C II	0.99	0.13	−0.10	0.60	0.98	1.6E–09	0.14
He II, C II	1.15	0.05	−0.41	0.23	0.94	1.3E–06	0.30
C IV, C II	0.93	0.12	0.76	0.55	0.98	1.4E–08	0.17
N V, C II	0.79	0.10	0.74	0.46	0.98	3.5E–09	0.15
Si IV, Mg II	0.92	0.38	−1.04	1.78	0.82	2.1E–03	0.44
He II, Mg II	0.97	0.13	−1.10	0.61	0.96	4.1E–06	0.23
C IV, Mg II	0.84	0.27	−0.15	1.31	0.85	8.4E–04	0.39
N V, Mg II	1.27	0.51	−2.73	2.42	0.80	3.4E–03	0.53
He II, Si IV	1.13	0.24	−0.17	1.07	0.94	1.9E–06	0.29
C IV, Si IV	0.93	0.06	0.89	0.26	0.96	1.1E–07	0.21
N V, Si IV	0.84	0.04	0.59	0.18	0.97	5.9E–08	0.17
C IV, He II	0.82	0.16	1.02	0.80	0.95	6.3E–07	0.25
N V, He II	0.67	0.13	1.07	0.64	0.92	7.4E–06	0.29
N V, C IV	0.85	0.06	0.08	0.29	0.99	4.9E–10	0.11

Note. Scaling relations are power laws of the form $\log_{10} F_{S,\ UV1} = m \times \log_{10} F_{S,\ UV2} + b$, where F_S is the surface flux in erg cm^{-2} s^{-1}, ρ is the Pearson correlation coefficient, n is the probability of no correlation, and σ is the standard deviation of the data points about the best-fit line (dex).

Table 10
UV Emission Line Scaling Relations with Stellar Rotation Period

UV	m	σ_m	b	σ_b	ρ	n	σ
Si III	−1.40	0.29	5.37	0.44	−0.86	7.3E–04	0.44
Lyα	−0.92	0.22	6.97	0.31	−0.86	7.5E–04	0.29
Si II	−0.85	0.13	3.93	0.18	−0.88	3.8E–04	0.28
C II	−1.37	0.29	5.49	0.44	−0.86	8.0E–04	0.44
Mg II	−1.18	0.15	6.52	0.23	−0.95	3.0E–05	0.25
Si IV	−1.32	0.30	5.31	0.45	−0.84	1.1E–03	0.43
He II	−1.26	0.19	5.52	0.27	−0.93	4.5E–05	0.30
C IV	−1.40	0.32	6.03	0.49	−0.82	1.9E–03	0.49
N V	−1.31	0.32	5.38	0.48	−0.81	2.5E–03	0.47

Note. Scaling relations are power laws of the form $\log_{10} F_{S,\ UV} = m$; $\times \log_{10} P_{rot} + b$, where F_S is the surface flux in erg cm^{-2} s^{-1} and P_{rot} is the rotation period in days, ρ is the Pearson correlation coefficient, n is the probability of no correlation, and σ is the standard deviation of the data points about the best-fit line (dex).

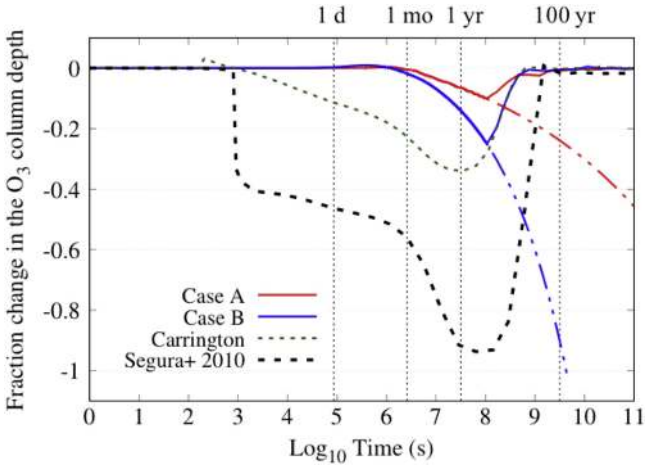

Figure 11. Fraction change in O_3 column depth as a function of time on a terrestrial planet with an Earth-like atmosphere and no magnetosphere (M. A. Tilley et al. 2017, in preparation). The four vertical dotted lines denote elapsed time of 1 day, 1 month, 1 yr, and 100 yr, respectively. Case A (solid red line) and Case B (solid blue line) represent the O_3 column depth for multiple proton impact events each with $\sim 1.2 \times 10^3$ pfu (a representative value for the flares discussed in Section 5.4) for a planet orbiting GJ 876 at 0.18 au. The frequencies of impact are 0.08 hr^{-1} for Case A and 0.5 hr^{-1} for Case B over a period of 40 months. The dot-dashed lines indicate a best fit to the behavior of the O_3 if the conditions for Case A and Case B were continued indefinitely as opposed to a period of 40 months. The dashed green line represents a single Carrington-class event (6.3×10^6 pfu at 0.18 au), and the dashed black line represents a single AD Leo great-flare-sized event (5.9×10^8 pfu at 0.16 au; Rodger et al. 2008; Segura et al. 2010).

1. Time-averaged Ca II K (3933 Å) residual equivalent width correlates positively with stellar surface flux of nine far- and near-UV emission lines, including H I Lyα (Table 5). The presented Ca II K and UV scaling relations allow for the UV spectrum of any M dwarf to be approximated from ground-based optical spectra.
2. We present a scaling relation between Ca II K equivalent width and the EUV spectrum for M dwarfs based on the Lyα–EUV scaling relations presented in Linsky et al. (2014) and the Ca II K–Lyα scaling relation determined in this work (Table 6). We estimate that the Ca II-based EUV fluxes are accurate within 40%.
3. We present a new method to estimate the energetic (>10 MeV) proton flux emitted during far-UV emission line flares (specifically Si IV $\lambda\lambda$1394, 1402 and He II λ1640; Table 7). The UV–proton scaling relations are derived from solar irradiance observations and in situ proton measurements near Earth.
4. We present methods to estimate the *GOES* flare classification corresponding to far-UV Si IV and He II ¯ares (Equations (8) and (9)). This is important for estimating the probability that any far-UV flare will have an accompanying proton enhancement. Larger solar flares have a higher probability of associated particle enhancements.
5. We analyze several flares observed with *Chandra* and *Hubble* from the M4 dwarf GJ 876 as part of the MUSCLES Treasury Survey and place the flare properties in context with solar flares (Section 5.4). We find that planets in GJ 876's HZ experience large, Carrington-like flares (soft X-ray flux $>10^{-3}$ W m^{-2}) and particle

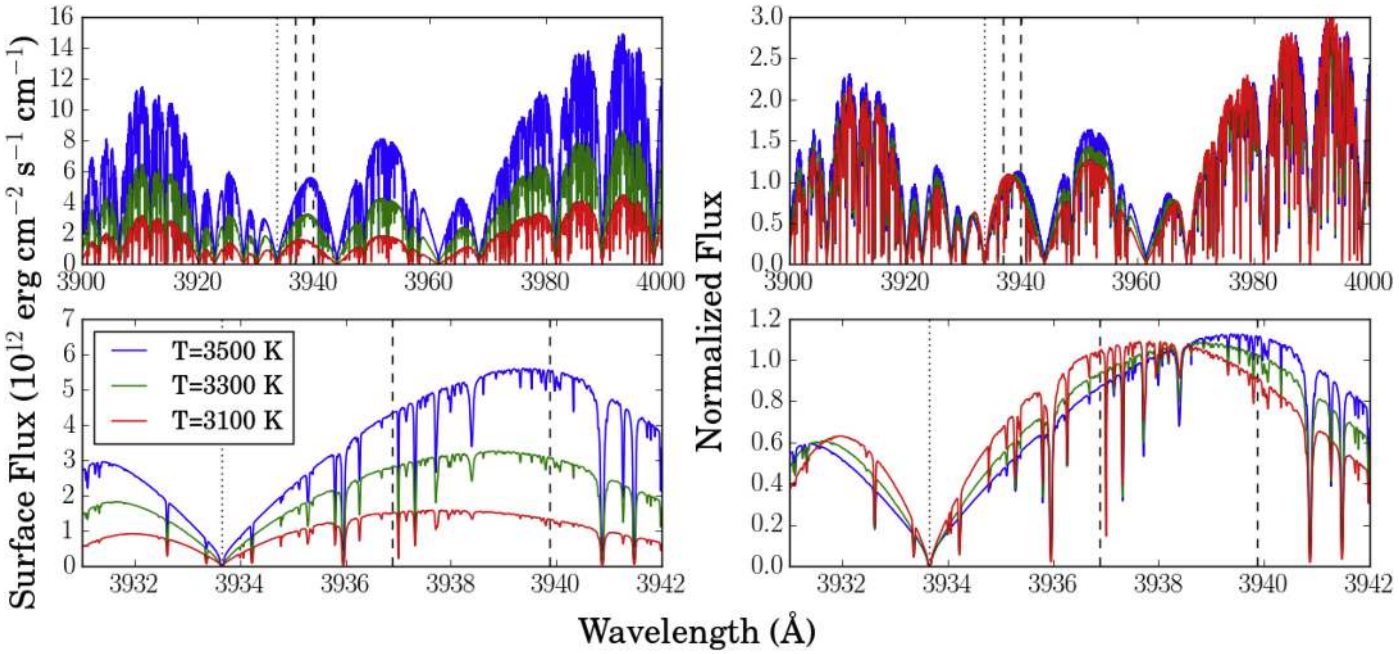

Figure 12. Ca II K photospheric absorption for three different M dwarf PHOENIX models—3100, 3300, and 3500 K (Husser et al. 2013). All models have $\log_{10} g = 5$ and [Fe/H] = 0 (solar). The vertical dotted black line shows the Ca II K line center (3933.66 Å), and the two vertical dashed lines show the continuum region (3936.9–3939.9 Å). The two left panels show the surface flux for the three different models, and the two right panels show the same models normalized to the average flux value in the continuum region.

enhancements approximately four orders of magnitude more frequently than Earth. Flare activity at the level observed on GJ 876 is predicted to lead to complete stripping of O_3 from an Earth-like planet on timescales between 10^2 and 10^5 yr.

M dwarfs are currently a prime target for exoplanet searches and characterization efforts with current and near-future technologies including *JWST*, but important questions have been raised about these planets' potential habitability. *JWST* will be able to characterize only a few M dwarf exoplanets, and we need to ensure that HZ terrestrial planets orbiting nearby M dwarfs with the maximum probability of hosting a detectable atmosphere are chosen for *JWST* target selection. The stellar host's UV SED and energetic particle flux are important drivers of chemistry, heating, and mass loss, but we do not have the space telescope resources for reconnaissance of every nearby M dwarf system, and energetic particles cannot be measured directly across interstellar distances. In this paper, we have provided tools to estimate UV SEDs from comparatively easy to obtain Ca II measurements and energetic particle fluxes from observed UV and X-ray flares.

The data presented here were obtained as part of the *HST* Guest Observing programs #12464 and #13650, as well as the COS Science Team Guaranteed Time programs #12034 and #12035. This work was supported by NASA grants *HST*-GO-12464.01 and *HST*-GO-13650.01 to the University of Colorado at Boulder. This work is also based on data from the *Chandra X-ray Observatory* (ObsIDs: 17315 and 17316) and supported by CXO grant G05-16155X. Observations were also obtained with the Apache Point Observatory 3.5 m telescope, which is owned and operated by the Astrophysical Research Consortium. This research has made extensive use of the Keck Observatory Archive (KOA), which is operated by the W. M. Keck Observatory and the NASA Exoplanet Science Institute (NExScI), under contract with the National Aeronautics and Space Administration. The ESO Science Archive Facility was also used to access VLT/XSHOOTER science products. This paper includes data gathered with the 6.5 m Magellan Telescopes located at Las Campanas Observatory, Chile. A.Y. thanks Don Woodraska for assistance with the *GOES* and *SDO*/EVE data, Juan Fontenla for providing the GJ 832 synthetic spectrum, and Lauren W. Blum for helpful discussions. E.R.N. acknowledges support from an NSF Astronomy and Astrophysics Postdoctoral Fellowship under award AST-1602597, and A.S. acknowledges the support of UNAM-PAPIIT project IN109015.

Facilities: *HST* (COS, STIS), ARC (DIS), CXO, Keck:I (HIRES), CASLEO:JST (REOSC), VLT:Kueyen (XSHOOTER), Magellan:Clay (MIKE), SDO (EVE), *GOES*.

Software: IRAF, Astropy (Robitaille et al. 2013), IPython (Perez & Granger 2007), Matplotlib (Hunter 2007), Pandas (McKinney 2010), NumPy and SciPy (van der Walt et al. 2011).

Appendix A
Equivalent Width Correction

The following exemplifies how a spectral type dependence is introduced in Ca II K equivalent width measurements and how it can be removed. See Figure 12 for examples on how the PHOENIX models used in Section 3 change as a function of spectral type.

Two stars, A and B, have different spectral types ($T_A > T_B$ and $R_A > R_B$) and are observed at different distances, d_A and

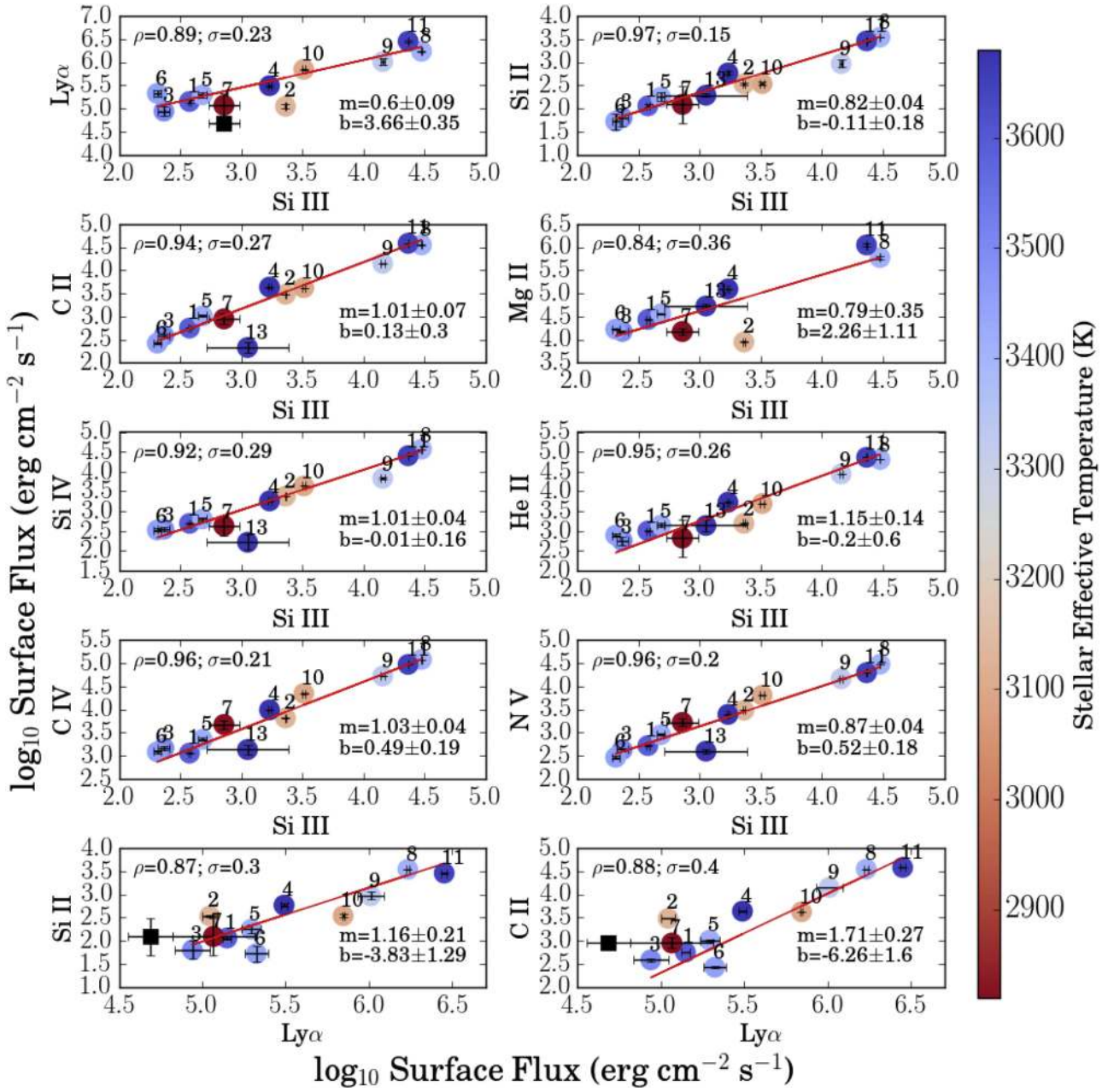

Figure 13. Surface fluxes (erg cm^{-2} s^{-1}) for the individual UV emission lines (see Tables 3 and 5). Each point represents a different star (numbered to match Table 2) color-coded by effective temperature. The black squares in the panels showing Lyα flux represent the uncorrected Lyα surface flux for GJ 1214 (see Youngblood et al. 2016). The data were fitted by power laws of the form $\log_{10} F_{S,UV1} = m \times \log_{10} F_{S,UV1} + b$, where $F_{S,UV}$ is the surface flux of the UV emission line in erg cm^{-2} s^{-1}. The fit coefficients m and b, the Pearson correlation coefficient ρ, and the standard deviation of the data points about the best-fit line σ (dex) are shown in each panel. GJ 1214 (star 7) was not included in any of the Lyα fits, but was included in all others.

d_B, from Earth. These stars have the same Ca II emission core surface flux (erg cm^{-2} s^{-1}), $F_{A,S} = F_{B,S}$, and therefore should have the same Ca II K equivalent widths, W_λ. From flux-calibrated Ca II spectra, we perfectly isolate the emission core from the observed line profile by fitting and subtracting a radiative equilibrium model, and we integrate over the residual Ca II K emission, finding $F_{A,S} \times R_A^2/d_A^2$ and $F_{B,S} \times R_B^2/d_B^2$ for Star A and Star B, respectively.

To convert the observed fluxes into equivalent widths, we normalize to nearby continuum, which has an average surface flux $x(T)$. Because Star A is warmer, $x(T_A) > x(T_B)$, and the resulting equivalent widths are not equal:

$$W_{\lambda,A} = \frac{F_{A,S} \times \frac{R_A^2}{d_A^2}}{x(T_A) \times \frac{R_A^2}{d_A^2}} = \frac{F_{A,S}}{x(T_A)}, \quad (10)$$

and

$$W_{\lambda,B} = \frac{F_{B,S} \times \frac{R_B^2}{d_B^2}}{x(T_B) \times \frac{R_B^2}{d_B^2}} = \frac{F_{B,S}}{x(T_B)}. \quad (11)$$

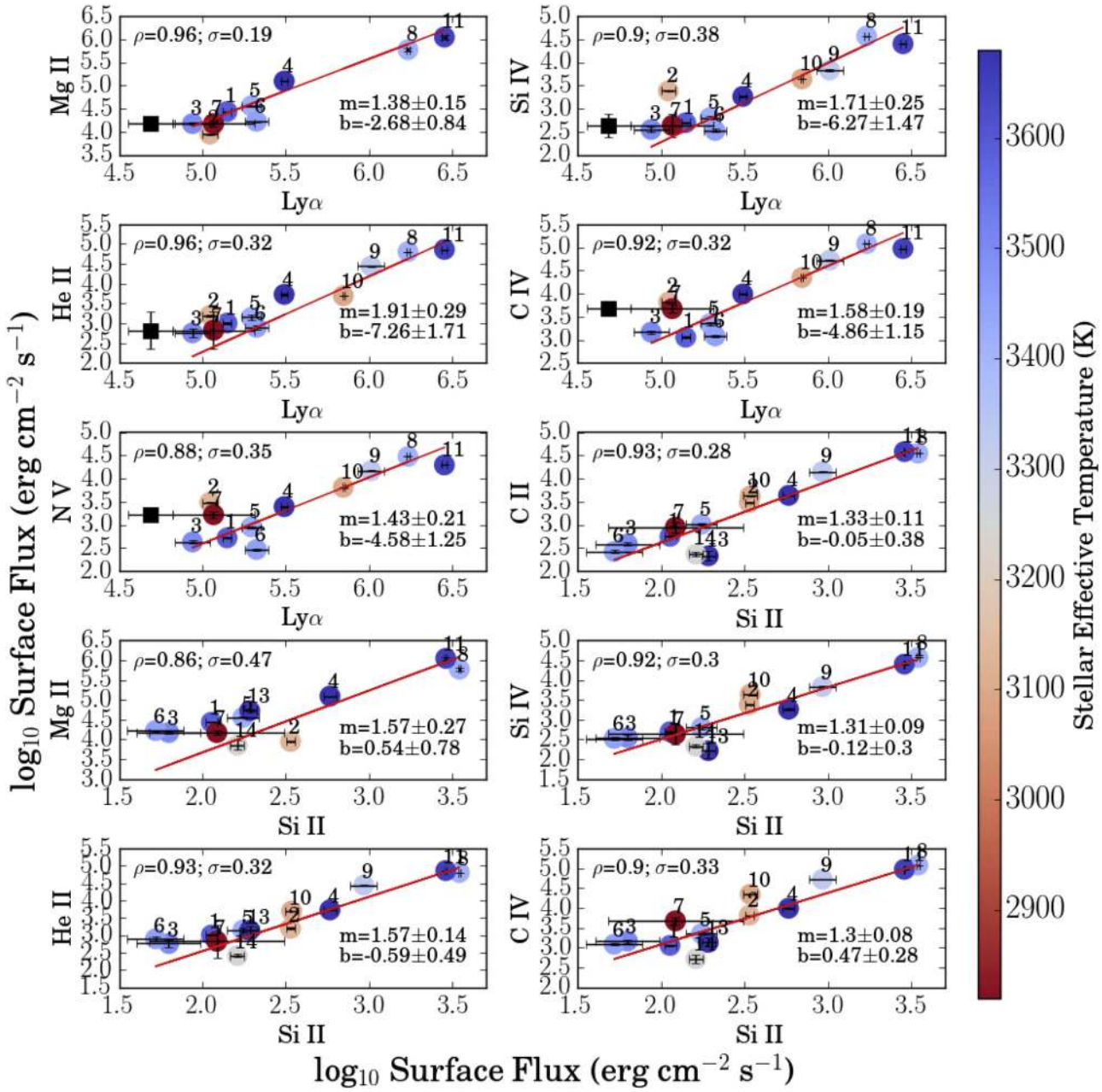

Figure 13. (Continued.)

To correct the equivalent widths so that they are equal for Star A and Star B, we multiply by $x(T)$ scaled to a reference value $x(T_{\rm ref})$. The "corrected" equivalent width is given by

$$W_{\lambda,\rm corr} = W_\lambda \times \frac{x(T)}{x(T_{\rm ref})}. \quad (12)$$

Figure 12 shows radiative equilibrium model spectra (PHOENIX; Husser et al. 2013) for three spectral subtypes from our sample—3100, 3300, and 3500 K. The cooler spectral subtypes have narrower Ca II absorption, as well as fainter continuum.

Appendix B
UV–UV Correlations

Here we present scaling relations between the nine far- and near-UV emission lines presented in Tables 3 and 5, and between these UV emission lines and the stellar rotation periods presented in Table 2. See Section 2.2 for a discussion of the UV spectra, including Lyα reconstructions and other corrections made for ISM absorption. All observed fluxes have been converted to surface fluxes using the stellar radii and distances presented in Table 2.

In Figure 13, we show the positive correlations between UV surface fluxes ($F_{\rm S,UV1}$, $F_{\rm S,UV2}$) and their power-law fits of the

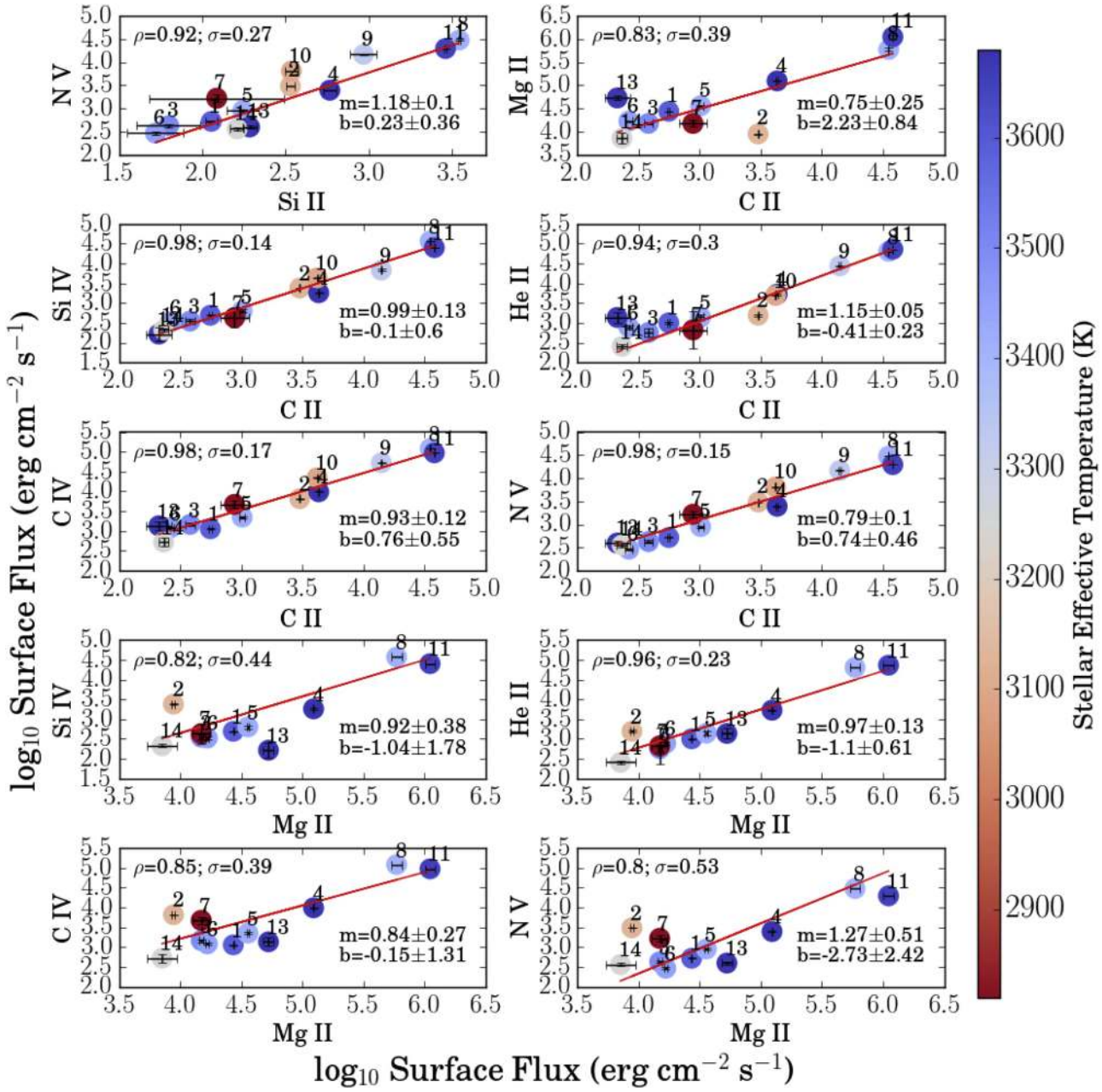

Figure 13. (Continued.)

form $\log_{10} F_{S,UV1} = m \times \log_{10} F_{S,UV2} + b$, which are also shown in Table 9. We find statistically significant correlations for all 36 combinations of the nine UV emission lines. The Pearson correlation coefficients range from 0.80 to 0.99, and the scatter about the best-fit lines ranges from 0.11 to 0.53 dex.

In Figure 14, we present the negative correlations between stellar rotation period (P_{rot}) and the nine UV emission lines with their power-law fits of the form $\log_{10} F_{S,\ UV1} = m \times \log_{10} P_{rot} + b$. The power-law fits are also shown in Table 10. All of the correlations are statistically significant, although our M dwarf sample is divided between two widely separated populations: $P_{rot} < 5$ days and $P_{rot} > 39$ days. Within the slowly rotating population or the fast-rotating population, most of the correlations are not statistically significant.

Youngblood et al. (2016) presented scaling relations between Lyα and Mg II, Si III, C IV, and P_{rot} for a smaller sample of M dwarfs. The shallow correlations ($m < 0.15$) found between Lyα and Si III and C IV were not statistically significant and were consistent with zero, likely due to the small sample size and the small range of explored parameter space. This work's power-law exponents between Lyα and Si III and C IV are $m = 0.60 \pm 0.09$ and $m = 0.63 \pm 0.08$, respectively, compared to the $m = 0.07 \pm 0.31$ and $m = 0.13 \pm 0.35$ values found by Youngblood et al. (2016). For Lyα and Mg II, our power-law exponent $m = 0.73 \pm 0.08$ is consistent with the $m = 0.77 \pm 0.10$ value from Youngblood et al. (2016), as is our exponent for the Lyα and P_{rot} relation: $m = -0.92 \pm 0.22$ compared to $m = -0.86 \pm 0.16$.

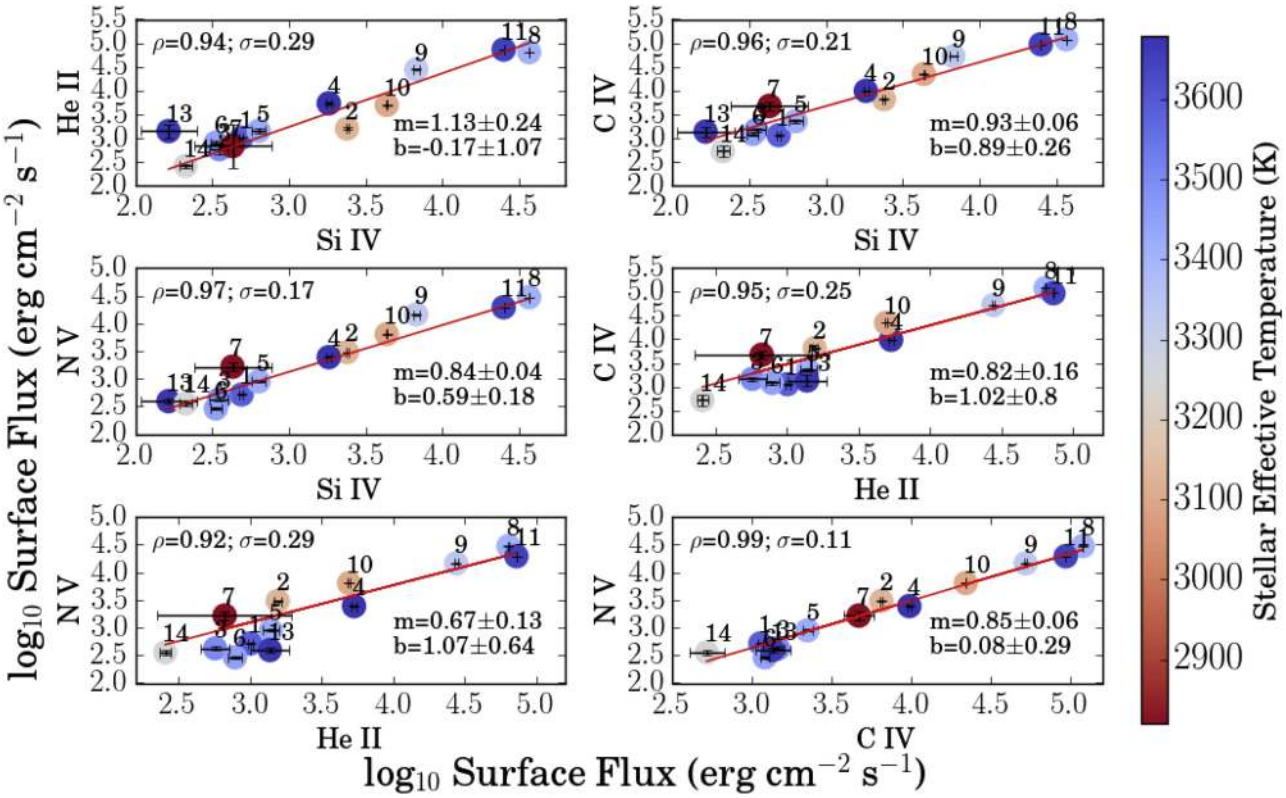

Figure 13. (Continued.)

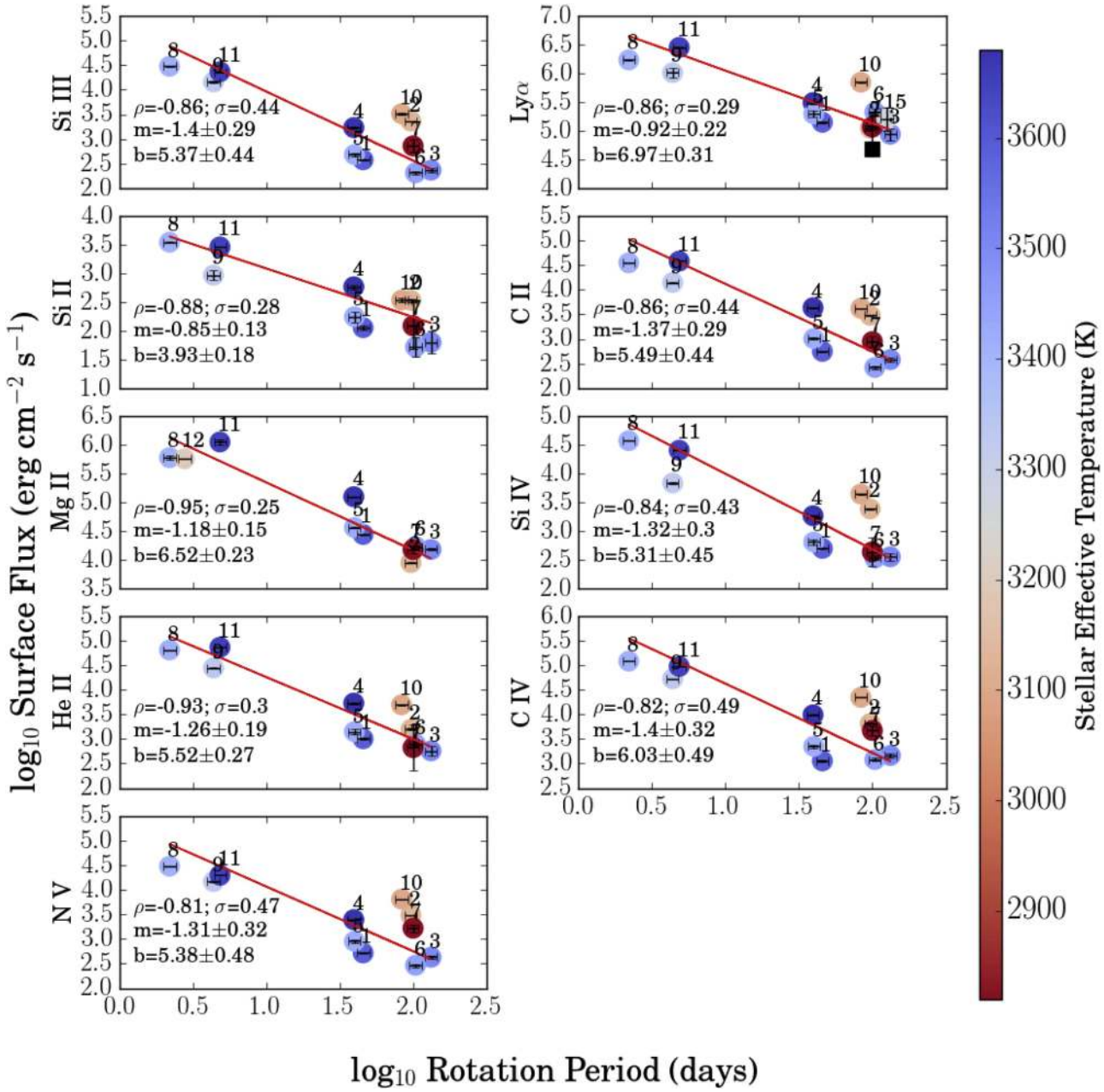

Figure 14. Surface fluxes (erg cm^{-2} s^{-1}) of the UV emission lines (see Tables 3 and 5) and the stellar rotation periods (days; Table 2). 10% error bars have been placed on the rotation periods. Each point represents a different star (numbered to match Table 2) color-coded by effective temperature. The black square in the top right panel represents the uncorrected Lyα surface flux for GJ 1214 (see Youngblood et al. 2016); GJ 1214 was not included in that panel's fit. The data were fitted by power laws of the form $\log_{10} F_{\rm S,UV} = m \times \log_{10} P_{\rm rot} + b$, where $F_{\rm S,UV}$ is the surface flux of the UV emission line in erg cm^{-2} s^{-1}, and $P_{\rm rot}$ is the rotation period in days. The fit coefficients m and b, the Pearson correlation coefficient ρ, and the standard deviation of the data points about the best-fit line σ (dex) are shown in each panel.

References

Airapetian, V. S., Glocer, A., Gronoff, G., Hébrard, E., & Danchi, W. 2016, NatGe, 9, 452
Anglada-Escudé, G., Rojas-Ayala, B., Boss, A. P., Weinberger, A. J., & Lloyd, J. P. 2013, A&A, 551, A48
Arney, G. N., Meadows, V. S., Domagal-Goldman, S. D., et al. 2017, ApJ, 836, 49
Barks, H. L., Buckley, R., Grieves, G. A., et al. 2010, ChemBioChem, 11, 1240
Belov, A., Garcia, H., Kurt, V., Mavromichalaki, H., & Gerontidou, M. 2005, SoPh, 229, 135
Belov, A., Kurt, V., Mavromichalaki, H., & Gerontidou, M. 2007, SoPh, 246, 457
Benedict, G. F., McArthur, B., Nelan, E., et al. 1998, AJ, 116, 429
Berta, Z. K., Charbonneau, D., Bean, J., et al. 2011, ApJ, 736, 12
Berta-Thompson, Z. K., Irwin, J., Charbonneau, D., et al. 2015, Natur, 527, 204
Bourrier, V., Ehrenreich, D., Wheatley, P. J., et al. 2017, A&A, 599, 3
Bourrier, V., Lecavelier des Etangs, A., Ehrenreich, D., Tanaka, Y. A., & Vidotto, A. A. 2016, A&A, 591, A121
Browning, M. K. 2008, ApJ, 676, 1262
Buccino, A. P., Petrucci, R., Jofré, E., & Mauas, P. J. D. 2014, ApJL, 781, L9
Busà, I., Aznar Cuadrado, R., Terranegra, L., Andretta, V., & Gomez, M. T. 2007, A&A, 466, 1089
Butler, C. J., Rodono, M., & Foing, B. H. 1988, A&A, 206, L1
Chabrier, G., & Küker, M. 2006, A&A, 446, 1027
Chadney, J., Galand, M., Unruh, Y., Koskinen, T., & Sanz-Forcada, J. 2015, Icar, 250, 357
Cincunegui, C., Díaz, R. F., & Mauas, P. J. D. 2007, A&A, 469, 309

Cincunegui, C., & Mauas, P. J. D. 2004, A&A, 414, 699
Cliver, E. W., & Dietrich, W. F. 2013, JSWSC, 3, A31
Cliver, E. W., Ling, A. G., Belov, A., & Yashiro, S. 2012, ApJL, 756, L29
Cohen, O., Drake, J. J., Glocer, A., et al. 2014, ApJ, 790, 57
Crosley, M. K., Osten, R. A., Broderick, J. W., et al. 2016, ApJ, 830, 24
Cully, S. L., Fisher, G. H., Abbott, M. J., & Siegmund, O. H. W. 1994, ApJ, 435, 449
Davenport, J. R. A., Kipping, D. M., Sasselov, D., Matthews, J. M., & Cameron, C. 2016, ApJL, 829, L31
Demory, B.-O., Ségransan, D., Forveille, T., et al. 2009, A&A, 505, 205
Dere, K. P., Landi, E., Mason, H. E., Monsignori Fossi, B. C., & Young, P. R. 1997, A&AS, 125, 149
Díaz, R. F., Cincunegui, C., & Mauas, P. J. D. 2007, MNRAS, 378, 1007
Dobler, W., Stix, M., & Brandenburg, A. 2006, ApJ, 638, 336
Domagal-Goldman, S. D., Segura, A., Claire, M. W., Robinson, T. D., & Meadows, V. S. 2014, ApJ, 792, 90
Domingo, V., Ermolli, I., Fox, P., et al. 2009, SSRv, 145, 337
Drake, J. J., Cohen, O., Garraffo, C., & Kashyap, V. 2016, in IAU Symp. 320, Solar and Stellar Flares and Their Effects on Planets, ed. A. Kosovichev, S. Hawley, & P. Heinzel (Cambridge: Cambridge Univ. Press), 196
Drake, J. J., Cohen, O., Yashiro, S., & Gopalswamy, N. 2013, ApJ, 764, 170
Dressing, C. D., & Charbonneau, D. 2015, ApJ, 807, 45
Fontenla, J., Witbrod, J., Linsky, J. L., et al. 2016, ApJ, 830, 154
Fontenla, J. M., Landi, E., Snow, M., & Woods, T. 2014, SoPh, 289, 515
Fossati, L., Marcelja, S. E., Staab, D., et al. 2017, A&A, 601, 104
France, K., Froning, C. S., Linsky, J. L., et al. 2013, ApJ, 763, 149
France, K., Linsky, J. L., Tian, F., Froning, C. S., & Roberge, A. 2012, ApJL, 750, L32
France, K., Loyd, R. O. P., Youngblood, A., et al. 2016, ApJ, 820, 89
Fuhrmeister, B., & Schmitt, J. H. M. M. 2004, A&A, 420, 1079
Gao, P., Hu, R., Robinson, T. D., Li, C., & Yung, Y. L. 2015, ApJ, 806, 249
Golding, T. P., Carlsson, M., & Leenaarts, J. 2014, ApJ, 784, 30
Golding, T. P., Leenaarts, J., & Carlsson, M. 2016, ApJ, 817, 125
Gomes da Silva, J., Santos, N. C., Bonfils, X., et al. 2011, A&A, 534, A30
Guinan, E. F., Engle, S. G., Durbin, A., et al. 2016, ApJ, 821, 81
Harman, C. E., Schwieterman, E. W., Schottelkotte, J. C., & Kasting, J. F. 2015, ApJ, 812, 137
Harra, L. K., Schrijver, C. J., Janvier, M., et al. 2016, SoPh, 291, 1761
Hawley, S. L., Davenport, J. R. A., Kowalski, A. F., et al. 2014, ApJ, 797, 121
Hawley, S. L., Gizis, J. E., & Reid, I. N. 1996, AJ, 112, 2799
Hawley, S. L., & Johns-Krull, C. M. 2003, ApJL, 588, L109
Hawley, S. L., & Pettersen, B. R. 1991, ApJ, 378, 725
Henry, T. J., Jao, W.-C., Subasavage, J. P., et al. 2006, AJ, 132, 2360
Henry, T. J., Kirkpatrick, J. D., & Simons, D. A. 1994, AJ, 108, 1437
Houdebine, E. R., Foing, B. H., & Rodono, M. 1990, A&A, 238, 249
Houdebine, E. R., Mullan, D. J., Paletou, F., & Gebran, M. 2016, ApJ, 822, 97
Hovestadt, D., Hoefner, H., Klecker, B., et al. 1981, ApJL, 246, L81
Hu, R., Seager, S., & Bains, W. 2012, ApJ, 761, 166
Hudson, H. S. 2007, ApJL, 663, L45
Hunter, J. D. 2007, CSE, 9, 90
Hunt-Walker, N. M., Hilton, E. J., Kowalski, A. F., Hawley, S. L., & Matthews, J. M. 2012, PASP, 124, 545
Husser, T.-O., Wende-von Berg, S., Dreizler, S., et al. 2013, A&A, 553, A6
Jao, W.-C., Henry, T. J., Subasavage, J. P., et al. 2005, AJ, 129, 1954
Jenkins, L. F. 1952, General Catalogue of Trigonometric Stellar Parallaxes (Hartford, CT: Yale Univ. Observatory)
Jordan, C. 1975, MNRAS, 170, 429
Kahler, S. W. 1982, JGR, 87, 3439
Kay, C., Opher, M., & Kornbleuth, M. 2016, ApJ, 826, 195
Kennedy, M. B., Milligan, R. O., Mathioudakis, M., & Keenan, F. P. 2013, ApJ, 779, 84
Kerwin, B. A., & Remmele, R. L. 2007, J. Pharm. Sci., 96, 1468
Kiplinger, A. L., & Garcia, H. A. 2004, BAAS, 36, 739
Kopparapu, R. K., Ramirez, R. M., SchottelKotte, J., et al. 2014, ApJL, 787, L29
Kraus, A. L., Tucker, R. A., Thompson, M. I., Craine, E. R., & Hillenbrand, L. A. 2011, ApJ, 728, 48
Krucker, S., & Lin, R. P. 2000, ApJL, 542, L61
Lammer, H., Lichtenegger, H. I. M., Kulikov, Y. N., et al. 2007, AsBio, 7, 185
Landi, E., Young, P. R., Dere, K. P., Del Zanna, G., & Mason, H. E. 2013, ApJ, 763, 86
Lingenfelter, R. E., & Hudson, H. S. 1980, in The Ancient Sun: Fossil Record in the Earth, Moon and Meteorites, ed. R. O. Pepin, J. A. Eddy, & R. B. Merrill (Oxford: Pergamon), 69
Linsky, J. L., Fontenla, J., & France, K. 2014, ApJ, 780, 61
Linsky, J. L., France, K., & Ayres, T. 2013, ApJ, 766, 69
Lorenzo-Oliveira, D., de Mello, G. F. P., Dutra-Ferreira, L., & Ribas, I. 2016, A&A, 595, A11
Loyd, R. O. P., & France, K. 2014, ApJS, 211, 9
Loyd, R. O. P., France, K., Youngblood, A., et al. 2016, ApJ, 824, 102
Luger, R., & Barnes, R. 2015, AsBio, 15, 119
Lurie, J. C., Henry, T. J., Jao, W.-C., et al. 2014, AJ, 148, 91
Marsden, S. C., Carter, B. D., & Donati, J.-F. 2009, MNRAS, 399, 888
Mason, J. P., Woods, T. N., Caspi, A., Thompson, B. J., & Hock, R. A. 2014, ApJ, 789, 61
Matsunaga, T., Hieda, K., & Nikaido, O. 1991, Photochem. Photobio., 54, 403
Mauas, P. J. D., Falchi, A., Pasquini, L., & Pallavicini, R. 1997, A&A, 326, 249
McCarthy, K., & White, R. J. 2012, AJ, 143, 134
McKinney, W. 2010, in Proc. 9th Python in Science Conf., ed. S. van der Walt & J. Millman, 51, http://conference.scipy.org/proceedings/scipy2010/mckinney.html
Miguel, Y., Kaltenegger, L., Linsky, J. L., & Rugheimer, S. 2015, MNRAS, 446, 345
Milligan, R. O., Kennedy, M. B., Mathioudakis, M., & Keenan, F. P. 2012, ApJL, 755, L16
Mitra-Kraev, U., Harra, L. K., Gdel, M., et al. 2005, A&A, 431, 679
Neves, V., Bonfils, X., Santos, N. C., et al. 2014, A&A, 568, A121
Newton, E. R., Irwin, J., Charbonneau, D., Berta-Thompson, Z. K., & Dittmann, J. A. 2016, ApJL, 821, L19
Noyes, R. W., Hartmann, L. W., Baliunas, S. L., Duncan, D. K., & Vaughan, A. H. 1984, ApJ, 279, 763
Osten, R. A., & Bastian, T. S. 2006, ApJ, 637, 1016
Osten, R. A., Kowalski, A., Drake, S. A., et al. 2016, ApJ, 832, 174
Osten, R. A., & Wolk, S. J. 2015, ApJ, 809, 79
Parker, E. N. 1958, ApJ, 128, 664
Patel, B. H., Percivalle, C., Ritson, D. J., Duffy, C. D., & Sutherland, J. D. 2015, NatCh, 7, 301
Perez, F., & Granger, B. E. 2007, CSE, 9, 21
Pettersen, B. R. 1980, AJ, 85, 871
Rauscher, E., & Marcy, G. 2006, PASP, 118, 617
Redfield, S., & Linsky, J. L. 2002, ApJS, 139, 439
Redfield, S., & Linsky, J. L. 2004, ApJ, 602, 776
Reiners, A., & Basri, G. 2008, A&A, 489, L45
Ribas, I., Bolmont, E., Selsis, F., et al. 2016, A&A, 596, A111
Ritson, D., & Sutherland, J. D. 2012, NatCh, 4, 895
Rivera, E. J., Lissauer, J. J., Butler, R. P., et al. 2005, ApJ, 634, 625
Robertson, P., Roy, A., & Mahadevan, S. 2015, ApJL, 805, L22
Robitaille, T. P., Tollerud, E. J., Greenfield, P., et al. 2013, A&A, 558, A33
Rodger, C. J., Verronen, P. T., Clilverd, M. A., Seppälä, A., & Turunen, E. 2008, JGR, 113, D23302
Roizman, G. S. 1984, SvAL, 10, 116
Rugheimer, S., Kaltenegger, L., Segura, A., Linsky, J., & Mohanty, S. 2015, ApJ, 809, 57
Sanz-Forcada, J., Micela, G., Ribas, I., et al. 2011, A&A, 532, A6
Scalo, J., Kaltenegger, L., Segura, A., et al. 2007, AsBio, 7, 85
Schrijver, C. J., Cote, J., Zwaan, C., & Saar, S. H. 1989, ApJ, 337, 964
Sciambi, R. K., Gloeckler, G., Fan, C. Y., & Hovestadt, D. 1977, ApJ, 214, 316
Segura, A., Kasting, J. F., Meadows, V., et al. 2005, AsBio, 5, 706
Segura, A., Krelove, K., Kasting, J. F., et al. 2003, AsBio, 3, 689
Segura, A., Meadows, V. S., Kasting, J. F., Crisp, D., & Cohen, M. 2007, A&A, 472, 665
Segura, A., Walkowicz, L. M., Meadows, V., Kasting, J., & Hawley, S. 2010, AsBio, 10, 751
Senanayake, S. D., & Idriss, H. 2006, PNAS, 103, 1194
Shields, A. L., Ballard, S., & Johnson, J. A. 2016, arXiv:1610.05765
Shine, R., Gerola, H., & Linsky, J. L. 1975, ApJL, 202, L101
Shkolnik, E. L., & Barman, T. S. 2014, AJ, 148, 64
Shkolnik, E. L., Rolph, K. A., Peacock, S., & Barman, T. S. 2014, ApJL, 796, L20
Suárez Mascareño, A., Rebolo, R., González Hernández, J. I., & Esposito, M. 2015, MNRAS, 452, 2745
Sun, X., Bobra, M. G., Hoeksema, J. T., et al. 2015, ApJL, 804, L28
Tevini, M. 1993, UV-B Radiation and Ozone Depletion: Effects on Humans, Animals, Plants, Microorganisms, and Materials (Boca Raton, FL: Lewis)
Thalmann, J. K., Su, Y., Temmer, M., & Veronig, A. M. 2015, ApJL, 801, L23
Tian, F., France, K., Linsky, J. L., Mauas, P. J., & Vieytes, M. C. 2014, E&PSL, 385, 22
Tilley, M. A., Harnett, E. M., & Winglee, R. M. 2016, ApJ, 827, 77
Tlatov, A. G., Dormidontov, D. V., Kirpichev, R. V., Pashchenko, M. P., & Shramko, A. D. 2015, Ge&Ae, 55, 961
van der Walt, S., Colbert, S. C., & Varoquaux, G. 2011, CSE, 13, 22

van Leeuwen, F. 2007, A&A, 474, 653
Vaughan, A. H., Preston, G. W., & Wilson, O. C. 1978, PASP, 90, 267
Venot, O., Rocchetto, M., Carl, S., Hashim, A. R., & Decin, L. 2016, ApJ, 830, 77
Veronig, A., Temmer, M., Hanslmeier, A., Otruba, W., & Messerotti, M. 2002, A&A, 382, 1070
Vidotto, A. A., Donati, J.-F., Jardine, M., et al. 2016, MNRAS, 455, L52
Voet, D., Gratzer, W. B., Cox, R. A., & Doty, P. 1963, Biopolymers, 1, 193
Vogt, S. S., Penrod, G. D., & Soderblom, D. R. 1983, ApJ, 269, 250
von Braun, K., Boyajian, T. S., Kane, S. R., et al. 2011, ApJL, 729, L26
von Braun, K., Boyajian, T. S., Kane, S. R., et al. 2012, ApJ, 753, 171
von Braun, K., Boyajian, T. S., van Belle, G. T., et al. 2014, MNRAS, 438, 2413
Walkowicz, L. M., & Hawley, S. L. 2009, AJ, 137, 3297
West, A. A., Weisenburger, K. L., Irwin, J., et al. 2015, ApJ, 812, 3
White, R. J., Schaefer, G., Ten Brummelaar, T., et al. 2015, BAAS, 225, 348.12
Wilson, O. C. 1978, ApJ, 226, 379
Winter, L. M., & Ledbetter, K. 2015, ApJ, 809, 105
Wood, B. E., Müller, H.-R., Redfield, S., & Edelman, E. 2014, ApJL, 781, L33
Wood, B. E., Müller, H.-R., Zank, G. P., Linsky, J. L., & Redfield, S. 2005a, ApJL, 628, L143
Wood, B. E., Redfield, S., Linsky, J. L., Muller, H., & Zank, G. P. 2005b, ApJS, 159, 118
Woods, T. N., Caspi, A., Chamberlin, P. C., et al. 2017, ApJ, 835, 122
Woods, T. N., Eparvier, F. G., Hock, R., et al. 2012, SoPh, 275, 115
Wordsworth, R., & Pierrehumbert, R. 2014, ApJL, 785, L20
Xie, H., Mäkelä, P., Gopalswamy, N., & St. Cyr, O. C. 2016, JGR, 121, 6168
Yadav, R. K., Christensen, U. R., Morin, J., et al. 2015, ApJL, 813, L31
Yashiro, S., Akiyama, S., Gopalswamy, N., & Howard, R. A. 2006, ApJL, 650, L143
Youngblood, A., France, K., Loyd, R. O. P., et al. 2016, ApJ, 824, 101